Published in final edited form as:
NMR Biomed. 2013 December ; 26(12): 1609–1629. doi:10.1002/nbm.3025.

Quantitative Proton Magnetic Resonance Techniques for Measuring Fat

Houchun Harry, Hu, Ph.D.[*] and
Department of Radiology, Children's Hospital Los Angeles, University of Southern California, Los Angeles, California, USA.

Hermien E. Kan, Ph.D.
C.J. Gorter Center for High Field MRI, Department of Radiology, Leiden University Medical Center, Leiden, The Netherlands.

Abstract

Accurate, precise, and reliable techniques for quantifying body and organ fat distributions are important tools in physiology research. They are critically needed in studies of obesity and diseases involving excess fat accumulation. Proton magnetic resonance methods address this need by providing an array of relaxometry-based (T_1, T_2) and chemical-shift-based approaches. These techniques can generate informative visualizations of regional and whole-body fat distributions, yield measurements of fat volumes within specific body depots, and quantify fat accumulation in abdominal organs and muscles. MR methods are commonly used to investigate the role of fat in nutrition and metabolism, to measure the efficacy of short and long-term dietary and exercise interventions, to study the implications of fat in organ steatosis and muscular dystrophies, and to elucidate pathophysiological mechanisms in the context of obesity and its comorbidities. The purpose of this review is to provide a summary of mainstream MR strategies for fat quantification. The article will succinctly describe the principles that differentiate water and fat proton signals, summarize advantages and limitations of various techniques, and offer a few illustrative examples. The article will also highlight recent efforts in MR of brown adipose tissue and conclude by briefly discussing some future research directions.

Keywords

fat quantification; white and brown adipose tissue; ectopic fat; muscle; obesity; water-fat MRI; spectroscopy; chemical-shift

INTRODUCTION

The development of accurate, precise, and reliable tools for quantifying triglyceride (fat) distribution throughout the body continues to evolve. These tools are critically needed as the prevalence of obesity, metabolic abnormalities, their comorbidities, and disease conditions

[*]**Corresponding Author** Houchun Harry Hu, PhD Children's Hospital Los Angeles University of Southern California 4650 Sunset Boulevard Department of Radiology, MS #81 Los Angeles, California, USA. 90027 hhu@chla.usc.edu, houchunh@usc.edu Office: +1 (323) 361-2688 Fax: +1 (323) 361-1510.

involving excess fat accumulation remain global health and socioeconomic concerns concern [1, 2] The quantification of adipose tissue and fat accumulation within organs and ectopic sites remains critical in physiological studies of obesity, metabolism, and nutrition, the metabolic syndrome, and their associated comorbidities. In addition to metabolic abnormalities, it is also important to monitor fat accumulation in conditions such as sarcopenia, muscular dystrophies and myelomeningocele, where skeletal muscle function and physical abilities can be affected. The buildup of fat in subcutaneous and visceral white adipose tissue (SCAT, VAT) depots, in conjunction with the deposition of fat in the liver, pancreas, heart, and skeletal muscles, are recognized determinants of one's metabolic health risk [3-5]. Ectopic fat refers to the deposition of triglycerides (TG) within cells of non-adipose tissue that typically contain only small amounts of fat. Thus, the liver, heart, pancreas, and skeletal muscles are all considered ectopic fat sites, where excessive fat accumulation can interfere with normal function. Quantitative magnetic resonance spectroscopy (MRS) and imaging (MRI) techniques are currently considered the most comprehensive tools for assessing body fat [6, 7].

Quantitative fat measurements can assist physicians with diagnosis, health risk assessment, and disease stratification in conditions such as neuromuscular disorders [8], fatty liver [9], and type II diabetes [10]. They can facilitate comparative studies in SCAT and VAT distributions between age, gender, and ethnicity groups [11, 12], and assist in understanding the pathophysiology of excessive fat accumulation. Longitudinal measurements can determine the efficacy of therapies and interventions aimed at altering body and organ TG levels, such as bariatric surgery [13], calorie-restricted diets [14-17], and physical exercise regimens [18]. Serial studies can also capture temporal changes in TG accumulation due to hyperalimentation [19] and the natural disease progression, such as in sarcopenia [20] and muscular dystrophies [21]. In the latter, MR can visualize preferential fat infiltration into specific muscles and highlight asymmetries between right and left legs. MRS has also been instrumental in quantifying small degrees of ectopic fat accumulation, particularly in the assessment of intramyocellular lipids in response to diet [22, 23] and exercise [24, 25], in both healthy subjects to understand normal physiology, and in those with impaired insulin sensitivity.

This review article was partly motivated by discussions at the 2012 ISMRM workshop on water-fat imaging (http://ismrm.org/workshops/FatWater12/). It is intended to provide the reader with a concise review of mainstream quantitative proton MR techniques available for fat assessment [26], including T_1- and T_2-weighted imaging methods, frequency-selective approaches, single-voxel MRS and chemical-shift imaging (CSI), and chemical-shift-encoded water-fat imaging (see Figure 1). The article will not attempt to review the pathophysiology of fat, as extensive commentaries and review articles already exist in the literature [3-5]. The technical descriptions will be presented in the context of white adipose tissue (WAT) and ectopic fat. Subsequently, recent investigations utilizing proton MRS and MRI to characterize brown adipose tissue (BAT) will be briefly summarized. The review will conclude with an outlook on future research directions.

QUANTITATIVE MR of FAT

Many approaches have been utilized for body fat assessment [27], including anthropometry metrics, hydrodensitometry, air displacement plethysmography, bioelectric impedance analysis, dual energy X-ray absorptiometry, X-ray CT [28-30], and quantitative magnetic resonance [31]. The utilization of MR has been steadily rising [32-36] and the modality is clearly emerging as a comprehensive tool for TG quantification [6, 7]. MR has been instrumental in identifying "at-risk" cohorts and those who exhibit benign forms of obesity [37, 38]. Table 1 provides an overview of mainstream MR techniques used in fat quantification, from T_1- and T_2-weighted methods, to MRS and CSI, frequency-selective MRI, and chemical-shift-encoded water-fat MRI approaches. In differentiating proton signals from water and fat, these aforementioned pulse sequences depend on either a difference in relaxometry alone (e.g. T_1, T_2), which usually manifests as a subsequent difference in tissue and organ signal intensities on the grayscale MR image [39], or additionally on a difference in chemical-shift and resonance frequency.

RELAXOMETRY-BASED APPROACHES

T_1-Weighted MRI—T_1-weighted pulse sequences have been utilized ubiquitously to quantify abdominal SCAT and VAT depots [28, 33-38], extramyocellular fat depots in the lower extremities [8, 32], fat deposits surrounding the heart as well as myocardial fat [40], and bone marrow adipose tissue [41]. The T_1 relaxation rate of fat is one of the shortest in vivo. Consequently, adipose tissue depots appear brightest on T_1-weighted images, facilitating identification. Using signal intensity histograms and thresholds [42], these depots can be delineated with relative ease and subsequently associated volumes can be computed [43]. The histogram and threshold processes are commonly applied in conjunction with shape-model constraints, edge-detection, clustering, and morphological (erosion, dilation) practices, and region-growing strategies to improve the accuracy of adipose tissue depot segmentations [44-48]. Additionally, pre-processing steps that correct for spatially-varying signal intensities in the image due to bias from non-uniform RF transmit and receive fields of the MR system are necessary, particularly at higher magnetic field strengths and in overweight/obese subjects [49]. Supplemental T_1 mapping can likewise aid in depot identification and segmentation [50]. Protocols reported in the literature range from the acquisition of a single abdominal axial slice to a stack of 2D slices for regional analysis [51] in the past, to advanced topographic whole-body volumes [52] for subject-specific characterization in more recent years. T_1-weighted imaging has also been extensively used in the assessment of fat in neuromuscular disorders [53, 54], where varying patterns of fat infiltration, asymmetric involvement, and preferential fat accumulation within specific muscles can be clearly depicted [55] (see Figure 2).

T_2-Weighted MRI—The T_2 relaxation rate of fat is neither the shortest nor the longest amongst tissue in vivo. On conventional T_2-weighted images, fat nonetheless appears bright, alongside fluid-filled structures that also appear hyperintense [39]. T_2-weighted protocols are not typically implemented for SCAT and VAT volume quantification. In lower extremity skeletal muscles however, the utility of quantitative T_2-weighted imaging, in combination with T_2 mapping, has been instrumental in the assessment of muscular fat deposition. In one

approach, a mono-exponential decay function is fitted voxel-by-voxel to the acquired signals from a multi-echo spin-echo pulse sequence to compute the T_2 relaxation rate. T_2 values above a threshold of 30-50 msec, which are typical for healthy muscle, are then likely indicative of the presence of fat [56, 57]. However, many muscle diseases are also characterized by edema, which in turn also increases the T_2 relaxation rate and can therefore confound the determination of fat deposition. To circumvent this ambiguity, bi-exponential and non-linear least squares techniques have been proposed, where voxel-wise fitting of the acquired multi-echo data results in individual signal intensities and T_2 values for lean muscle tissue, edema, and fat components [58, 59]. Figure 3 illustrates an example of this approach in a patient with facioscapulohumeral muscular dystrophy. One recognized advantage of quantitative T_2 fitting and mapping techniques in comparison to conventional qualitative T_1 and T_2-weighted imaging is the reduction of partial volume effects and quantification errors in voxels situated at the interface of muscle and adipose tissue. This benefit is particularly important since fat accumulation within skeletal muscles can be heterogeneous, and in some instances to a degree where high spatial resolution protocols may still be inadequate in resolving fat patterns.

CHEMICAL-SHIFT BASED APPROACHES

MR Spectroscopy and Chemical-Shift Imaging—Proton MR spectroscopy and chemical-shift imaging provide the most direct approach to discriminate water and fat signals in vivo and have long been considered the non-invasive gold-standard for ectopic fat quantification. The differences in Larmor resonance frequencies between water and fat protons are used to spectrally separate them. The reader is referred to several exemplary illustrations of the water-fat spectrum in recent literature [60-63]. While water is a symmetrical molecule with a single proton resonance (-OH), the TG spectrum is more complex and has several resonances. In addition to the major methylene ($-CH_2-$) resonance, the spectrum is characterized by additional minor peaks, reflecting other proton moieties and various non-identical local magnetic fields. MRS has been widely used to measure fat deposition in the liver [61, 64], heart [14, 65], and pancreas [66], as well as in skeletal muscle [67-70] and in bone marrow [71-73]. One recognized advantage of spectroscopy is its ability to accurately quantify very low amounts of fat [74].

The detailed frequency spectrum of water and fat resonance peaks provides an intuitive visualization of the presence of water and fat proton moieties within the interrogated voxel. The relative area under each spectral peak can also be quantified to reflect water and fat content. Assessment of the ratios of the ensemble of fat resonances can provide information on TG properties, including the level of carbon chain unsaturation [75, 76]. Spectral analysis can be performed using software available on the MR system or offline with dedicated packages [77, 78]. Automated software on MR systems can perform basic post-processing steps like noise filtering, baseline phase correction, and simple peak fitting to determine water and fat levels. Commercial packages provide users with advanced levels of data handling, such as spectral modeling via multiple weighted overlapping Gaussian or Lorenzian distributions. For multi-coil data, combination algorithms have also been described [79, 80]. The common quantitative endpoint from spectral analysis is a T_2-corrected fat-signal fraction [60, 63, 64], computed as the sum of the areas under all

quantifiable fat peaks divided by the sum of the water and fat peak areas. T_1 effects are usually mitigated during data acquisition by employing a long repetition time. Subject motion, respiratory and cardiac motion, and abdominal peristalsis can easily degrade spectrum quality. Breath-hold enabled protocols, dedicated pulse sequences with motion navigators, and respiratory and cardiac triggered data acquisition schemes remain essential practices, especially in the thorax and abdomen [81, 82].

In research and clinical practices, both single-voxel MRS and multi-voxel CSI are used. The two most widely used single-voxel approaches are the Stimulated Echo Acquisition Mode [83] and Point RESolved Spectroscopy [84] pulse sequences. Techniques that are more robust to chemical-shift displacement artifacts have also been introduced [85-87]. In single-voxel MRS, a series of slice-selective RF pulses are applied sequentially to excite a volume-of-interest. This is subsequently followed by data acquisition of an echo in the time domain in the absence of spatial-encoding gradients. Compared to voxels in MRI, MRS voxels are an order of magnitude bigger in size. Volumes ranging from 5-20 milliliters are common. While this is beneficial from a signal-to-noise ratio (SNR) perspective and enhances greater detection sensitivity to small fat concentrations, it requires accurate voxel placement to avoid any undesired adjacent tissues and structures. For example, in liver and pancreas applications, the interrogating voxel must exclude major blood vessels, the gallbladder and biliary structures, and adjacent VAT [88]. In skeletal muscle applications, voxel placement is likewise critical in order to distinguish intra- (IMCL) and extra- myocellular lipids (EMCL) [89].

In CSI phase encoding steps precede data acquisition [90] to provide a multi-voxel grid of spectra, as illustrated in Figure 4. While CSI scan times can be on the order of tens of minutes, they are becoming more manageable with fast echo-planar-imaging k-space trajectories and parallel imaging [91], and emerging compressed sensing strategies [92, 93]. Voxel sizes in CSI are typically on the order of one milliliter. Major advantages of CSI over single-voxel MRS are the possibility to capture heterogeneous fat accumulation across a larger area of anatomy and that the placement of the grid of imaging voxels is less dependent on the MR operator. However, voxel boundary definition in CSI is not as sharp as in single-voxel MRS, and signal bleeding from neighboring voxels can influence quantitative accuracy if spatial variations in fat concentrations are significant. For example, in skeletal muscles, adjacent subcutaneous and intermuscular adipose tissue depots can significantly influence IMCL quantification [94]. Technical advances in outer volume suppression [95] and pulse sequence strategies [96] have been introduced to mitigate some of these challenges.

Presently, spectroscopy remains the only method that can differentiate IMCL and EMCL in skeletal muscle (see Figure 4), due to the very small difference in resonance frequency between these two lipid components [97, 98]. In healthy skeletal muscle, normal IMCL content varies from 2-5% by volume. Similar to brown adipocytes (described later), IMCL exists as spherical droplets in the cytoplasm within myocytes and the chemical-shift location of its methylene resonance is independent of the orientation of the surrounding skeletal muscle fibers with respect to the external B0 magnetic field. In contrast, EMCL exists between skeletal muscle fibers and between muscle fiber and fascia boundaries in the form

of structured parallel sheaths. Consequently for EMCL, a bulk magnetic susceptibility is present and the degree of susceptibility is dependent on the orientation of the EMCL compartment with respect to the external B0 magnetic field. For example, for a subject positioned supine within the MR scanner with their legs extended and flat on the table, the methylene resonance position of EMCL is maximally shifted from that of IMCL in the tibialis anterior muscle, of which the muscle fibers are aligned in parallel with the external magnetic field. By comparison, in the soleus muscle, in which the fibers are oriented in an angle of approximately 40 degrees to the main magnetic field, the susceptibility-induced chemical-shift is minimal and consequently the methylene resonances of IMCL and EMCL partly overlap. Voxel placement is therefore critical when quantifying IMCL, as EMCL levels are typically greater than the intrinsic concentration of IMCL and the amplitude of the EMCL signal relative to the IMCL signal can vary significantly depending on the voxel location [99]. In overweight/obese subjects and at lower magnetic field strengths, spectral peak overlaps can occur more frequently, hindering IMCL and EMCL quantification. While the likelihood of peak overlaps can be mitigated by utilizing long echo times [100], additional signal corrections (e.g. T_2) are needed to maintain quantitative accuracy [60, 63, 64].

The role of IMCL in normal human physiology and in disease has been extensively studied. While EMCL is metabolically inactive and serves primarily as a site of TG storage, IMCL can be metabolized to provide an energy source for muscle activity. Hence, baseline IMCL levels can vary significantly between subjects and within a subject throughout the day. IMCL levels are influenced by many factors including gender [101], physical activity [102], and diet [103-105]. Obese, sedentary, and diabetic patients typically have high IMCL levels and low insulin sensitivity [67]. In trained athletes however, a paradox exists where both high IMCL levels and high insulin sensitivity have been observed [106]. In contrast, lower IMCL levels have been observed in healthy adults who are predisposed to familial longevity [107]. The rate of IMCL depletion by exercise has been shown to depend on the type and duration of exercise performed, the type of muscle fibers involved, and the level of baseline IMCL prior to the onset of exercise [25]. Conversely, the rate of IMCL replenishment is influenced by factors such as the percent fat content in the consumed diet and insulin levels [108].

Frequency-Selective Imaging—The chemical-shift phenomenon between water and fat protons that underpins spectroscopy can be extended to MRI. Consider a simplified single-peak spectral model of fat that includes only the methylene peak, in addition to the signal from the water resonance. In frequency-selective MRI, frequency-tuned RF pulses are used to either excite or suppress water or fat proton signals prior to data acquisition, in a manner similar to magnetization preparation schemes [109-114]. In one approach, spectral-spatial RF pulses are applied to selectively excite either the water or the methylene fat protons prior to data acquisition. The resultant image reflects only signals from the component that was spectrally excited. In another strategy, frequency-selective RF pulses are first applied to suppress signals from water or methylene protons. Subsequently, signals from the non-suppressed component are acquired for image formation.

The utility of fat-selective excitation has been demonstrated in the quantification of lower-extremity skeletal muscle percent fat content [115]. Water-suppression techniques have also been explored as a complementary method for quantifying SCAT, VAT, and intermuscular WAT volumes [116, 117]. Frequency-selective protocols have also been reported in the liver [118, 119] to measure hepatic fat-signal fractions and the method has been further demonstrated as an effective strategy in providing complementary and comprehensive abdominal fat assessment [120]. Frequency-selective strategies are often coupled to conventional T_1- and T_2-weighted protocols. Water versus fat signal contrast is typically stronger with frequency-selectivity since one component signal is being actively excluded by RF pulses. Figure 5 and Figure 6 demonstrate frequency-selective MRI in a bilayer water-oil phantom and in vivo, respectively. Figure 6 alludes to the issue of magnetic field inhomogeneity, also known as B0 off-resonance effects. This refers to spatially-varying deviations of the magnetic field, which can cause unintentional resonance frequency drifts on the order of 10^2 to 10^3 Hz. Inhomogeneities arise from manufacturing imperfections, perturbations by metallic implants, patient and physiological motion, and the mere placement of a human body inside the magnet bore. They can be significant around abdominal air-tissue-bowel interfaces and can cause an RF pulse designed to target fat to erroneously affect water. Conversely, an RF pulse intended to suppress water can inadvertently affect fat [121].

Chemical-Shift-Encoded Water-Fat Imaging—Chemical-shift-encoded water-fat imaging, heretofore referred to as water-fat MRI (WFI), integrates two-component water-fat spectral detection with high spatial resolution 2D and 3D MRI [122, 123]. In contrast to frequency-selective methods, WFI strategies do not employ RF pulses to selectively excite or suppress signals. Rather, two or more echoes are acquired to capture snapshots of the chemical-shift effect, manifested as a phase difference between water and fat signals. Subsequently in data reconstruction, elegant mathematical algorithms are used to solve and separate the individual water and fat components from the acquired data based on spectral model assumptions [124] and various parameter constraints. With the water and fat signals separated on a voxel-wise basis, a resultant fat-signal fraction map can be computed. A toolbox containing a sampling of some WFI algorithms can be found at the 2012 ISMRM workshop website (http://ismrm.org/workshops/FatWater12/data.htm). In both WFI and spectroscopy, the chemical-shift differences between water and fat resonances and the number of resonance peaks of fat are typically constrained in data reconstruction. One distinction is that the relative amplitudes of the water and fat peaks are assigned a priori in WFI algorithms, whereas in spectroscopy they are estimated from spectral data fitting as free parameters. In WFI, the preset water-fat spectrum is substituted into the reconstruction algorithms as either a single-fat (methylene)-peak model or as a multi-fat-peak model [61, 76, 125], the latter providing improved accuracy in fat-signal fraction estimations.

The concept of WFI emerged in the early-1980s [126-128]. By adopting the single-fat-peak model, Dixon introduced the notion of “simple spectroscopic imaging” with in-phase and out-of-phase echo times. Figure 7 illustrates the utility of in-phase/out-of-phase (e.g. two-point) WFI in highlighting the presence of ectopic fat [9, 129]. In recent years, this approach and its multi-echo variants have rapidly advanced to become popular tools in the

quantitative assessment of body and ectopic fat distributions [71, 119, 130-140]. Numerous methodological developments in WFI have also advanced the original two-point approach to afford more flexible echo time choices [141, 142] and improve the robustness of water-fat reconstructions, particularly in the presence of significant B0 magnetic field inhomogeneity [143-145]. Modern three and six-point WFI acquisitions, coupled with magnitude and complex-based algorithms [146], have also overcome multiple challenges including tissue susceptibility [147] and bipolar gradient readout schemes [148]. The general trend towards multi-echo WFI stems from the principle need to mathematically solve a multitude of unknown parameters, including water (real or complex value), fat (real or complex value), magnetic field inhomogeneity (real value), and T_2* relaxation rate (real value). The T_2* parameter is considered a confounder in the context of quantitative WFI [149]. However, it is worth mentioning that the parameter itself is clinically useful as an adjunct biomarker to assess iron overload [150-152]. Conversely, the presence of fat has also been argued as a confounder in the accurate estimation of T_2* [153]. The requisite number of echoes in WFI is largely governed by the number of unknown parameters in a particular water-fat signal model, while leveraging performance tradeoffs in noise-bias, SNR, and numerical stability of the reconstruction algorithms. The accuracy and precision of estimating the fat-signal fraction from WFI acquisitions have also been thoroughly investigated and improved upon significantly by strategies that employ multi-peak spectral model of fat [154-156] and those that explicitly account for confounding factors such as T_1 and T_2* relaxation effects on the water and fat signals [157, 158]. By addressing these confounders, it has been posited that the resultant proton-density fat fraction represents a fundamental property of the underlying tissue [159] and that it is a reliable imaging biomarker of tissue fat content [160]. As illustrated in Figure 8, this biomarker provides a powerful tool for visualizing ectopic fat distributions. Figure 9 shows a schematic of multi-echo gradient-echo WFI. Table 1 summarizes the principles, advantages and disadvantages, and typical endpoints of all of the aforementioned relaxometry and chemical-shift based quantitative MR techniques.

BROWN ADIPOSE TISSUE

The adipose organ is composed not only of WAT, but also BAT [161-163]. Recent findings of metabolically active BAT with positron emission and computed tomography (PET/CT) [164, 165] have led to a resurgence of scientific interest in the tissue's role in human physiology and developmental growth. Presently, PET/CT remains the reference modality in BAT imaging. The depiction of metabolically active BAT by PET/CT relies on the uptake of a radiotracer. The typical radiotracer is 18F-fluorodeoxyglucose, while other compounds linked to 11-Carbon [166] and 15-Oxygen [167] have been explored. In rodents, BAT can be found prominently in the interscapular region, located dorsal and inferior to the animal's shoulders [168, 169]. In humans, BAT in the supraclavicular fossa and cervical depots are the most commonly observed and reported sites in the PET/CT literature, while other anatomical sites have also been documented in detailed post-mortem studies [170-172]. WAT and BAT exhibit different morphological features. WAT is characterized by large adipocytes that contain a unilocular TG vacuole, a displaced peripheral nucleus, and limited intracellular water and extracellular space. In contrast, BAT typically contains smaller adipocytes with multiple TG droplets, a centrally located nucleus, and an abundance of iron-

rich mitochondria and intracellular water. WAT and BAT also exhibit different metabolic activity. Whereas WAT stores fat and is typically inactive, BAT can be stimulated to metabolize fat and generate heat. Thermogenesis is mediated by a unique uncoupling protein residing in the brown adipocyte's mitochondrial membrane. Unlike WAT, BAT can be densely perfused by capillaries, and such vascularity is needed to transport and disperse the produced heat [173]. As will be described shortly, these intrinsic differences between BAT and WAT provide the basis for a variety of signal contrast mechanisms in MR. MR represents a promising modality to overcome some of the challenges of utilizing PET/CT to study BAT, most notably in healthy pediatric and adult cohorts.

Table 2 identifies works in MR of BAT and summarizes major efforts in this area over the past two decades. The publications have been grouped based on the primary MR technique(s) employed and as well as each study's focus on measuring either BAT morphology and/or metabolic activity. The table also distinguishes whether the work was investigated in ex vivo specimens, animals, or humans, and the magnetic field strength at which the experiments were implemented. The significance of each study's findings is also noted. In general, the development of MR methods to image BAT is still at its infancy and has to date primarily focused on demonstrating technique feasibility in relatively small cohorts. While methodological studies have traditionally been implemented in rodents, those involving humans have started to emerge in the past five years. However, clinical case reports describing the identification of hibernomas as BAT [174-178], the involvement of BAT in pheochromocytoma [179], and the observation of BAT [180], have been quite common.

In comparison to lean muscle and TG-rich WAT, the mixed content of water and fat in BAT and its implications on the tissue's signal intensity and appearance in conventional T_1- and T_2-weighted images have long been recognized in rodents [181-184] and humans [179, 180]. In one recent study using a multi-echo fast-spin-echo pulse sequence, WAT was shown to exhibit a significantly higher T_2 distribution than BAT [184]. The longer tissue T_2 of WAT is likely due to the greater TG and lower intracellular water contents of white adipocytes in comparison to brown adipocytes. The reader may find that this trend is logical and synonymous to the aforementioned knowledge that skeletal muscle T_2 increases with greater fat accumulation [56-59]. Hamilton, et al. has employed MRS to further measure and compare the T_1 and T_2 values of water and the individual TG resonances between BAT and WAT, demonstrating only a noticeable difference in the water T_1 relaxation rate between the two tissues [185].

The mixture of water and fat content in BAT most logically extends to applications of fat-signal fraction MR. Both spectroscopy [60, 185, 186] and frequency-selective MRI [187-189] have been used to posit the concept that BAT generally has a lower fat-signal fraction than WAT. Over the past five years, the extension of WFI techniques to reinforce this concept has been demonstrated consistently in mice [190-193] and humans [194-201]. Preliminary comparisons between WFI and PET/CT of BAT are also beginning to emerge [195, 198, 201], bringing forth the reasonable notion that a negative PET/CT result for BAT implies that the tissue is either metabolically inactive or that the tissue is absent, and that with additional MR-derived fat-signal fraction measurements, the two conditions can

potentially be further differentiated. It should be noted that measurements of fat-signal fraction does not necessarily reflect BAT mass or volume. Rather, it is an additional signal-based characterization of the adipose tissue depot. One recognized advantage of fat-signal fraction BAT imaging is that proton spectroscopy and frequency-selective pulse sequences are readily available from commercial vendors in the current research and clinical environments. In addition, rapid 3D WFI techniques are becoming more widely accessible. This has been instrumental in allowing multiple investigators to independently verify the utility of the fat-signal fraction in differentiating BAT from WAT and in characterizing BAT morphology. The strategy's main drawback however is that the intermediate fat-signal fraction range is not unique to BAT and is only suggestive of the presence of the tissue. Even at a sub-millimeter spatial resolution, fat-signal fraction measurements alone can not differentiate a depot of brown adipocytes from a mixed cluster of brown and white adipocytes. The latter scenario is unfortunately quite common in humans [161, 169-172]. In abnormal circumstances where ectopic fat has infiltrated organs and skeletal muscles, or alternatively in normal situations such as conversion of red to yellow bone marrow, regional fat-signal fraction values are likely similar to the range occupied by BAT. Thus, knowledge of anatomy remains is needed to identify BAT depots and it is for this reason that all of the aforementioned reports have focused on large and easily recognizable BAT depots in rodents (interscapular, peri-renal) and humans (supraclavicular fossa, cervical). This limitation also extends to the two extremes of the fat-signal fraction range. A fat-depleted brown adipocyte will exhibit a near-zero percent fat-signal fraction, which can be ambiguous with adjacent lean tissues. Conversely, a fat-replenished brown adipocyte will exhibit a near-one-hundred percent fat-signal fraction, which can be false-positively identified as WAT. Thus, despite its growing popularity in recent years, the fat-signal fraction metric has notable limitations and is likely only one of several yet undiscovered complementary MR biomarkers that can collectively and reliably identify BAT in vivo.

Advanced proton spectroscopy techniques have also been employed to further characterize BAT. In a recent mouse study, an innovative strategy utilizing intermolecular zero-quantum coherence transitions between water and fat protons was described to differentiate BAT from WAT [202]. The approach exploited the fact that in brown adipocytes, intracellular water and fat are in close proximity to one another and thus give rise to distinctive signal peaks along the intermolecular coherence spectrum. On the contrary, in WAT, water and fat molecules are separated by slightly greater distances and thus such signal peaks can be rendered absent based on specific pulse sequence gradient settings. One critical advantage of intermolecular coherence spectroscopy is its insensitivity to partial-volume effects. The approach can unambiguously detect the presence of BAT since the generated signals rely on water and fat molecular interactions at the tissue microstructure level. The feasibility of intermolecular coherence spectroscopy at clinical magnetic field strengths of 1.5 Tesla and 3.0 Tesla in both rodents and humans has not yet been demonstrated. Challenges include the need to optimize the method for SNR at these field strengths and to accelerate data acquisition speed to a duration suitable for human studies.

It is worthwhile at this point to emphasize that human BAT imaging with MR is fundamentally challenging. In contrast to rodents where distinct clusters of “pure” brown adipocytes exist, in humans BAT is notably present in scattered distribution and often exists

in much smaller islets that are typically co-populated with white adipocytes [161, 169-172]. Thus, it is likely reasonable to imply that rodent depots (e.g. interscapular) are occupied largely by brown adipocytes, and that imaging-derived measurements of depot volume and mass can be interpreted as a close approximation of underlying BAT volume and mass. Conversely in humans, the high potential of mixed appearances of brown adipocytes with other cells presents a challenge in explicitly determining BAT volume and mass. BAT volume and mass cannot be reliably inferred from measurements of the resident depot volume and mass (e.g. supraclavicular fossa, cervical). This is because currently available fat-signal fraction methods are hampered by partial-volume effects and can not readily determine the percentage of brown and white adipocytes and other cells within the depots. Thus, the benefits and capability of a combined intermolecular coherence spectroscopy and WFI approach [203] would be highly desirable in advancing human BAT measurements.

SUMMARY

The preceding sections have firstly summarized MR techniques for quantifying TG (fat) distributions in the body (see Table 1). It is worth reiterating that the fat-signal fraction computed from frequency-selective MRI, spectroscopy, and WFI are generally weighted by intrinsic signal relaxation effects (e.g. T_1, T_2, T_2*) and is typically not equivalent to the proton-density fat fraction [159] or more conventional mass fat fraction or volume fat fraction [204]. It is also worth reemphasizing that presently MR spectroscopy remains the only technique with the sensitivity to differentiate IMCL and EMCL. Secondly, recent efforts to characterize BAT morphology and metabolic activity with some of these aforementioned MR techniques have been reviewed (see Table 2). The reader should find it apparent that the intrinsic intracellular differences in water and fat content between BAT and WAT lends naturally to characterization and assessment by quantitative fat MR techniques. In the following section, some opportunities for future investigations are identified.

OUTLOOK

Future Directions for WAT MR

For body fat composition of WAT depots and ectopic fat, the time-consuming task associated with post-processing image segmentation should be addressed. While many innovative and automated algorithms continue to emerge [205, 206], one challenge is that they are often limited to in-house usage and applicable to only a specific set of imaging protocols that generate a particular type of tissue signal contrast. Some of these algorithms are often difficult to obtain for a majority of end-users such as investigators of obesity and body composition, who may not necessarily be experts in imaging or image data processing. A structure for open-source sharing of segmentation algorithms and an effort by the imaging community towards standardization of protocols and procedures is recommended. With respect to studies of neuromuscular disorders, there remains a need to investigate the preferential deposition of fat between muscle groups and within muscle groups, as well as intra- and inter-subject differences. MR can enable such studies and facilitate analysis of fat pattern recognition for disease diagnosis [55, 136]. Automated muscle segmentation likewise needs to be addressed and recent efforts have shown promise [117, 207-210]. Validation of such algorithms in patient cohorts is needed. Additional strategies such as

diffusion-tensor imaging [211, 212] are also needed to complement fat in tracking disease progression and assessing muscle integrity, volume, and function.

The temporal redistribution of body and organ fat due to weight changes, diet and exercise, and bariatric surgery, along with its implications in insulin and glucose regulation, cardiovascular diseases, and other co-morbidities of obesity, remain critical research areas. Fat redistribution trends during adolescence, menopause, and aging as a function of normal physiology also remain unclear. Additionally, progress towards depot-specific fat quantification is needed, beyond the current practice of demarcating SCAT and VAT compartments [26, 163]. For example, it has been shown that the abdominal SCAT depot is partitioned into two distinct compartments [213] and it has been speculated that the deep layer is associated with negative health risks [214], possibly due to lower TG unsaturation levels [215]. The utility of determining variations in fatty acid composition across multiple locations of the body using MRS has been recognized [7, 216], and initial feasibility of obtaining such data with imaging techniques has been shown [62, 63, 217].

There is an unmet need to develop non-invasive imaging techniques that can assess adipocytes at the molecular level, such as monitoring adipocyte macrophage inflammation [218], cell number and density, and cell size [189]. When cell size increases, it is an indication of the inability of pre-existing adipocytes to expand further in number to accommodate extra TG accumulation [219, 220]. Larger adipocytes are likely associated with greater VAT and ectopic fat, and macrophage accumulation is associated with greater fasting insulin levels and hindered beta-cell function [221, 222]. Ultra-small-paramagnetic-iron-oxide particles [223] and diffusion-weighted spectroscopy [224] and imaging [225] of fat may offer a viable approach to characterizing adipose tissue microstructure. Lastly, it remains unknown whether enlarged WAT depots exist as a result of decreased TG oxidation, increased TG uptake, or a structural imbalance between uptake and expenditure. The measurement of the metabolic flux of fat with 13-Carbon MRS [105, 226] has enabled the opportunity to assess fat dynamically in a single imaging session. With oral ingestion or intravenous infusion of TG enriched with 13-Carbon, it is possible to monitor the uptake, turnover, deposition, and overall kinetics of triglyceride metabolism.

Future Directions for BAT MR

Leveraging on the existing knowledge of human BAT from PET/CT data, it is become increasingly evident that BAT fulfills an important, complex, and yet still largely unknown role in human physiology. The clinical relevance of BAT and its therapeutic potential, if any, remains unclear. Continued development of MR-based strategies to characterize human BAT morphology and metabolic activity, along with the independent validation and utilization of these strategies in large cohorts, are critically needed. Both the fat-signal fraction imaging and the intermolecular coherence spectroscopy approaches have only recently been validated independently by select research groups. Whereas MR protocols for quantifying WAT and organ fat are ubiquitous have become broadly accepted, presently it remains unclear, in the opinion of the first-author, whether routine measurements of BAT will become equally established in human studies. As illustrated in Figure 10, recent advances in PET/MR technology holds potential as an adjunct tool for combined

morphological and functional BAT imaging, with reduced radiation exposure than the status quo of PET/CT. Furthermore, a whole-body WFI scan is required in PET/MR to provide tissue attenuation correction maps for the PET signal detectors.

Many distinctive features of BAT are known and are only beginning to be explored with MR. In addition to intracellular fat and water levels, BAT metabolic activity can be probed by established perfusion techniques such as arterial-spin-labeling and contrast-enhanced MRI [227]. Figure 11 illustrates the visualization of BAT with Gadolinium MR angiography, highlighting the tissue's rich vascularity. Within this context, the sensitivity of dynamic T_2*-weighted blood-oxygen-level-dependent (BOLD) MRI techniques in quantifying BAT activity due to norepinephrine stimulation has been reported in mice [228]. It was demonstrated that an increase in BAT metabolic activity is accompanied by an increase in oxygen consumption and consequently a greater level of deoxyhemolgobin in the local blood flow. A decrease in venous and overall BAT T_2* follows, leading to a characteristic reduction in tissue signal intensity that confirms previous observations [183]. Additionally in rodents, the feasibility of utilizing T_2-weighted protocols and innovative iron-based blood pool contrast agents to assess tissue perfusion, in conjunction with a novel beta-adrenergic receptor agonist to stimulate BAT, has been described [184]. The capability of T_2*-weighted BOLD MRI to monitor hemodynamic fluctuations in response to BAT metabolic activity, without the use of an exogenous contrast agent, has also been extended to young adults with cold-exposure activation [201]. The use of advanced multi-echo WFI techniques to jointly yield complementary fat-signal fraction and T_2* metrics also remains a directions of future work [191, 195, 196, 198, 200]. Alternatively, potential differences in diffusion rates of water and fat molecules between BAT and WAT [225, 226], temperature mapping techniques [229], and magnetization transfer effects, have not yet been explored.

As summarized in the lower portion of Table 2, MR strategies utilizing other nuclei, including hyperpolarized 13-Carbon [230, 231] and 129-Xenon [232, 233] have shown tremendous promise as biomarkers in quantifying BAT metabolic activity in mice over the past year. Their application in humans remains strong avenues of possibility. Additionally, several spectroscopy reports have reported appreciable variations in TG unsaturation levels between BAT and WAT in rodent studies [60, 75, 185, 186]. The underlying sources of this difference in unsaturation levels need to be investigated in the context of metabolism and nutrition, and in humans. Aforementioned WFI-based approaches that are capable of characterizing TG properties [62, 63, 217] can be potentially useful in this context.

Lastly, recent efforts have identified human BAT as a distinct type of thermogenic fat cell, and have since referred to this admixed phenotype as “beige” or “brite (brown-in-white)” adipocytes [197, 234, 235]. MR approaches that can differentiate classical brown from “beige” adipocytes remains to be developed. This is undoubtedly challenging as many of the currently identified differences between brown and “beige” adipocytes reside at the cellular and genetic levels. The reader may have also inadvertently noticed that the cellular descriptions of IMCL in skeletal myocytes and brown adipocytes are remarkably similar. The two cell types share many common features, including an abundance of mitochondria and vascular perfusion, energy expenditure via oxidative phosphorylation, uncoupling proteins, and sympathetic innervation. Elucidating the associations between BAT and

muscle, especially in the context of energy expenditure, remains another provocative direction of research [236]. Lastly, the pathophysiology of WAT and the consequences of its excess accumulation within the body have been extensively documented. Whereas the central focus has been traditionally on WAT, research emphasis should consider shifting the paradigm to include BAT. Backed by innovative imaging methods, the role of BAT in all aspects human physiology can begin to be explored [237-240].

CONCLUSION

In conclusion, MR is a powerful and comprehensive imaging tool for body fat quantification. With a variety of established and emerging techniques, research studies will continue to demonstrate MR's flexible utility in fat assessment and characterization. Many aspects of fat's role in normal human physiology and disease remain for future investigations. With this review, the authors have aimed to provide the reader with sufficient materials and literature references in quantitative fat MR, in both the technical underpinnings and the clinical research applications.

Acknowledgments

The authors are grateful for their research funding supports. Due to space restrictions, the authors were unable to include many references that have undoubtedly contributed to this vast field. This is particularly true for Table 2 and the topic of brown adipose tissue, where the field is advancing rapidly and new publications are emerging steadily in both the basic science and imaging literature. The authors thank their colleagues and the readers for their understanding, and apologize for any unintentional omissions.

Funding and Research Support

To HH Hu

- National Institutes of Health / NIDDK – K25DK087931

- James H. Zumberge Research and Innovation Fund, University of Southern California

- Children's Hospital Los Angeles receives research support from Philips Healthcare.

To HE Kan

- Consultancy support from Prosensa Therapeutics BV. No personal fees are received.

All payments are made to the Leiden University Medical Center.

- The C.J. Gorter Center receives research support from Philips Healthcare.

ABBREVIATIONS

BAT	brown adipose tissue
BOLD	blood-oxygen-level-dependent
CSI	chemical shift imaging
CT	computed tomography
EMCL	extramyocellular lipid
IMCL	intramyocellular lipid

PET	positron emission tomography
SCAT	subcutaneous adipose tissue
SNR	signal-to-noise ratio
TG	triglyceride
VAT	visceral adipose tissue
WAT	white adipose tissue
WFI	water-fat MRI

REFERENCES

1. Ogden CL, Carroll MD, Kit BK, Flegal KM. Prevalence of obesity and trends in body mass index among US children and adolescents, 1999-2010. JAMA. 2012; 307:483–490. [PubMed: 22253364]
2. McAllister EJ, Dhurandhar NV, Keith SW, Aronne LJ, Barger J, Baskin M, Benca RM, Biggio J, Boggiano MM, Eisenmann JC, Elobeid M, Fontaine KR, Gluckman P, Hanlon EC, Katzmarzyk P, Pietrobelli A, Redden DT, Ruden DM, Wang C, Waterland RA, Wright SM, Allison DB. Ten putative contributors to the obesity epidemic. Crit Rev Food Sci Nutr. 2009; 49:868–913. [PubMed: 19960394]
3. Smith SR, Lovejoy JC, Greenway F, Ryan D, deJonge L, de la Bretonne J, Volafova J, Bray GA. Contributions of total body fat, abdominal subcutaneous adipose tissue compartments, and visceral adipose tissue to the metabolic complications of obesity. Metabolism. 2001; 50:425–435. [PubMed: 11288037]
4. Eckel RH, Grundy SM, Zimmet PZ. The metabolic syndrome. Lancet. 2005; 365:1415–1428. [PubMed: 15836891]
5. Després JP, Lemieux I, Bergeron J, Pibarot P, Mathieu P, Larose E, Rodés-Cabau J, Bertrand OF, Poirier P. Abdominal obesity and the metabolic syndrome: contribution to global cardiometabolic risk. Arterioscler Thromb Vasc Biol. 2008; 28:1039–1049. [PubMed: 18356555]
6. van der Meer RW, Lamb HJ, Smit JW, de Roos A. MR imaging evaluation of cardiovascular risk in metabolic syndrome. Radiology. 2012; 264:21–37. [PubMed: 22723560]
7. Machann J, Horstmann A, Born M, Hesse S, Hirsch FW. Diagnostic imaging in obesity. Best Pract Res Clin Endocrinol Metab. 2013; 27:261–277. [PubMed: 23731887]
8. Wattjes MP, Kley RA, Fischer D. Neuromuscular imaging in inherited muscle diseases. Eur Radiol. 2010; 20:2447–2460. [PubMed: 20422195]
9. Reeder SB, Cruite I, Hamilton G, Sirlin CB. Quantitative assessment of liver fat with magnetic resonance imaging and spectroscopy. J Magn Reson Imaging. 2011; 34:729–749. [PubMed: 21928307]
10. Lee Y, Lingvay I, Szczepaniak LS, Ravazzola M, Orci L, Unger RH. Pancreatic steatosis: harbinger of type 2 diabetes in obese rodents. Int J Obes (Lond). 2010; 34:396–400. [PubMed: 20010902]
11. Samara A, Ventura EE, Alfadda AA, Goran MI. Use of MRI and CT for fat imaging in children and youth: what have we learned about obesity, fat distribution and metabolic disease risk? Obes Rev. 2012; 13:723–732. [PubMed: 22520361]
12. Staiano AE, Katzmarzyk PT. Ethnic and sex differences in body fat and visceral and subcutaneous adiposity in children and adolescents. Int J Obes (Lond). 2012; 36:1261–1269. [PubMed: 22710928]
13. Hernandez TL, Kittelson JM, Law CK, Ketch LL, Stob NR, Lindstrom RC, Scherzinger A, Stamm ER, Eckel RH. Fat redistribution following suction lipectomy: defense of body fat and patterns of restoration. Obesity (Silver Spring). 2011; 19:1388–1395. [PubMed: 21475140]

14. van der Meer RW, Hammer S, Smit JW, Frölich M, Bax JJ, Diamant M, Rijzewijk LJ, de Roos A, Romijn JA, Lamb HJ. Short-term caloric restriction induces accumulation of myocardial triglycerides and decreases left ventriciular diastolic function in healthy subjects. Diabetes. 2007; 56:2849–2853. [PubMed: 17717279]
15. Lim EL, Hollingsworth KG, Aribisala BS, Chen MJ, Mathers JC, Taylor R. Reversal of type 2 diabetes: normalization of beta cell function in association with decreased pancreas and liver triacylglycerol. Diabetologia. 2011; 54:2506–2014. [PubMed: 21656330]
16. Snel M, Jonker JT, Hammer S, Kerpershoek G, Lamb HJ, Meinders AE, Pijl H, de Roos A, Romijn JA, Smit JW, Jazet IM. Long-term beneficial effect of a 16-week very low calorie diet on pericardial fat in obese type 2 diabetes mellitus patients. Obesity (Silver Spring). 2012; 20:1572–1576. [PubMed: 22282049]
17. Lee S, Bacha F, Hannon T, Kuk JL, Boesch C, Arslanian S. Effects of aerobic versus resistance exercise without caloric restriction on abdominal fat, intrahepatic lipid, and insulin sensitivity in obese adolescent boys: a randomized, controlled trial. Diabetes. 2012; 61:2787–2795. [PubMed: 22751691]
18. Machann J, Thamer C, Stefan N, Schwenzer NF, Kantartzis K, Häring HU, Claussen CD, Fritsche A, Schick F. Follow-up whole-body assessment of adipose tissue compartments during a lifestyle intervention in a large cohort at increased risk for type 2 diabetes. Radiology. 2010; 257:353–363. [PubMed: 20713612]
19. Erlingsson S, Herard S, Dahlqvist Leinhard O, Lindström T, Länne T, Borga M, Nyström FH. Men develop more intraabdominal obesity and signs of the metabolic syndrome after hyperalimentation than women. Metabolism. 2009; 58:995–1001. [PubMed: 19394660]
20. Cesari M, Fielding RA, Pahor M, Goodpaster B, Hellerstein M, Van Kan GA, Anker SD, Rutkove S, Vrijbloed JW, Isaac M, Rolland Y, M'rini C, Aubertin-Leheudre M, Cedarbaum JM, Zamboni M, Sieber CC, Laurent D, Evans WJ, Roubenoff R, Morley JE, Vellas B. Biomarkers of sarcopenia in clinical trials-recommendations from the International Working Group on Sarcopenia. J Cachexia, Sarcopenia and Muscle. 2012; 3:181–190. [PubMed: 22865205]
21. Fischmann A, Hafner P, Fasler S, Gloor M, Bieri O, Studler U, Fischer D. Quantitative MRI can detect subclinical disease progression in muscular dystrophy. J Neurol. 2012; 259:1648–654. [PubMed: 22297459]
22. Lê KA, Faeh D, Stettler R, Ith M, Kreis R, Vermathen P, Boesch C, Ravussin E, Tappy L. A 4-wk high-fructose diet alters lipid metabolism without affecting insulin sensitivity or ectopic lipids in healthy humans. Am J Clin Nutr. 2006; 84:1374–1379. [PubMed: 17158419]
23. Lee S, Boesch C, Kuk JL, Arslanian S. Effects of an overnight intravenous lipid infusion on intramyocellular lipid content and insulin sensitivity in African American versus Caucasian adolescents. Metabolism. 2013; 62:417–423. [PubMed: 23122836]
24. Zehnder M, Ith M, Kreis R, Saris W, Boutellier U, Boesch C. Gender-specific usage of intramyocellular lipids and glycogen during exercise. Med Sci Sports Exerc. 2005; 37:1517–1524. [PubMed: 16177603]
25. Vermathen P, Saillen P, Boss A, Zehnder M, Boesch C. Skeletal muscle 1H MRSI before and after prolonged exercise. I. muscle specific depletion of intramyocellular lipids. Magn Reson Med. 2012; 68:1357–1367. [PubMed: 22287260]
26. Shen W, Wang Z, Punyanita M, Lei J, Sinav A, Kral JG, Imielinska C, Ross R, Heymsfield SB. Adipose tissue quantification by imaging methods: a proposed classification. Obes Res. 2003; 11:5–16. [PubMed: 12529479]
27. Mattsson S, Thomas BJ. Development of methods for body composition studies. Phys Med Biol. 2006; 51:R203–228. [PubMed: 16790904]
28. Seidell JC, Bakker CJ, van der Kooy K. Imaging techniques for measuring adipose-tissue distribution--a comparison between computed tomography and 1.5-T magnetic resonance. Am J Clin Nutr. 1990; 51:953–957. [PubMed: 2349931]
29. Goodpaster BH, Thaete FL, Kelley DE. Composition of skeletal muscle evaluated with computed tomography. Ann N Y Acad Sci. 2000; 904:18–24. [PubMed: 10865705]

30. Lubura M, Hesse D, Neumann N, Scherneck S, Wiedmer P, Schurmann A. Non-invasive quantification of white and brown adipose tissues and liver fat content by computed tomography in mice. PLoS One. 2012; 7:e37026. [PubMed: 22615880]

31. Napolitano A, Miller SR, Murgatroyd PR, Coward WA, Wright A, Finer N, De Bruin TW, Bullmore ET, Nunez DJ. Validation of a quantitative magnetic resonance method for measuring human body composition. Obesity (Silver Spring). 2008; 16:191–198. [PubMed: 18223634]

32. Schick F, Machann J, Brechtel K, Strempfer A, Klumpp B, Stein DT, Jacob S. MRI of muscular fat. Magn Reson Med. 2002; 47:720–727. [PubMed: 11948733]

33. Machann J, Thamer C, Schnoedt B, Haap M, Häring HU, Claussen CD, Stumvoll M, Fritsche A, Schick F. Standardized assessment of whole body adipose tissue topography by MRI. J Magn Reson Imaging. 2005; 21:455–462. [PubMed: 15778954]

34. Siegel MJ, Hildebolt CF, Bae KT, Hong C, White NH. Total and intraabdominal fat distribution in preadolescents and adolescents: measurement with MR imaging. Radiology. 2007; 242:846–856. [PubMed: 17244720]

35. Kullberg J, Karlsson AK, Stokland E, Svensson PA, Dahlgren J. Adipose tissue distribution in children: automated quantification using water and fat MRI. J Magn Reson Imaging. 2010; 32:204–210. [PubMed: 20575078]

36. Silver HJ, Niswender KD, Kullberg J, Berglund J, Johansson L, Bruvold M, Avison MJ, Welch EB. Comparison of gross body fat-water magnetic resonance imaging at 3 Tesla to dual-energy X-ray absorptiometry in obese women. Obesity (Silver Spring). 2013; 21:765–774. [PubMed: 23712980]

37. Stefan N, Kantartzis K, Machann J, Schick F, Thamer C, Rittig K, Balletshofer B, Machicao F, Fritsche A, Häring HU. Identification and characterization of metabolically benign obesity in humans. Arch Intern Med. 2008; 168:1609–1616. [PubMed: 18695074]

38. Thomas EL, Parkinson JR, Frost GS, Goldstone AP, Dore CJ, McCarthy JP, Collins AL, Fitzpatrick JA, Durighel G, Taylor-Robinson SD, Bell JD. The missing risk: MRI and MRS phenotyping of abdominal adiposity and ectopic fat. Obesity (Silver Spring). 2012; 20:76–87. [PubMed: 21660078]

39. Bitar R, Leung G, Perng R, Tadros S, Moody AR, Sarrazin J, McGregor C, Christakis M, Symons S, Nelson A, Roberts TP. MR pulse sequences: what every radiologist wants to know but is afraid to ask. Radiographics. 2006; 26:513–537. [PubMed: 16549614]

40. Kellman P, Hernando D, Arai AE. Myocardial fat imaging. Curr Cardiovasc Imaging Rep. 2010; 3:83–91. [PubMed: 20401158]

41. Shen W, Chen J, Gantz M, Punyanitya M, Heymsfield SB, Gallagher D, Albu J, Engelson E, Kotler D, Pi-Sunyer X, Gilsanz V. MRI-measured pelvic bone marrow adipose tissue is inversely related to DXA-measured bon mineral in younger and older adults. Eur J Clin Nutr. 2012; 66:983–988. [PubMed: 22491495]

42. Wittsack HJ, Kapitza C, Cohnen M, Jung G, Heinemann L, Mödder U, Poll L. Interactive thresholded volumetry of abdominal fat using breath-hold T1-weighted magnetic resonance imaging. Rofo. 2006; 178:810–815. [PubMed: 16862508]

43. Shen W, Wang Z, Tang H, Heshka S, Punyanitya M, Zhu S, Lei J, Heymsfield SB. Volume estimates by imaging methods: model comparisons with visible woman as the reference. Obes Res. 2003; 11:217–225. [PubMed: 12582217]

44. Positano V, Gastaldelli A, Sironi AM, Santarelli MF, Lombardi M, Landini L. An accurate and robust method for unsupervised assessment of abdominal fat by MRI. J Magn Reson Imaging. 2004; 20:684–689. [PubMed: 15390229]

45. Liou TH, Chan WP, Pan LC, Lin PW, Chou P, Chen CH. Fully automated large-scale assessment of visceral and subcutaneous abdominal adipose tissue by magnetic resonance imaging. Int J Obes (Lond). 2006; 30:844–852. [PubMed: 16418756]

46. Kullberg J, Johansson L, Ahlström H, Courivaud F, Koken P, Eggers H, Börnert P. Automated assessment of whole-body adipose tissue depots from continuously moving bed MRI: a feasibility study. J Magn Reson Imaging. 2009; 30:185–193. [PubMed: 19557740]

47. Dahlqvist Leinhard O, Johansson A, Rydell J, Smedby Ö , Nyström F, Lundberg P, Borga M. Quantitative abdominal fat estimation using MRI. IEEE 19th International Conference on Pattern Recognition.. 2008; 19:1–4.
48. Wald D, Teucher B, Dinkel J, Kaaks R, Delorme S, Boeing H, Seidensaal K, Meinzer HP, Heimann T. Automatic quantification of subcutaneous and visceral adipose tissue from whole-body magnetic resonance images suitable for large cohort studies. J Magn Reson Imaging. 2012; 36:1421–1434. [PubMed: 22911921]
49. Würslin C, Springer F, Yang B, Schick F. Compensation of RF field and receiver coil induced inhomogeneity effects in abdominal MR images by a prior knowledge of the human adipose tissue distribution. J Magn Reson Imaging. 2011; 34:716–726. [PubMed: 21769975]
50. Kullberg J, Angelhed JE, Lonn L, Brandberg J, Ahlström H, Frimmel H, Johansson L. Whole-body T1 mapping improves the definition of adipose tissue: consequences for automated image analysis. J Magn Reson Imaging. 2006; 24:394–401. [PubMed: 16786577]
51. Maislin G, Ahmed MM, Gooneratne N, Thorne-Fitzgerald M, Kim C, Teff K, Arnardottir ES, Benediktsdottir B, Einarsdottir H, Juliusson S, Pack AI, Gislason T, Schwab RJ. Single slice vs. volumetric MR assessment of visceral adipose tissue: reliability and validity among the overweight and obese. Obesity (Silver Spring). 2012; 20:2124–2132. [PubMed: 22395811]
52. Würslin C, Machann J, Rempp H, Claussen C, Yang B, Schick F. Topography mapping of whole body adipose tissue using a fully automated and standardized procedure. J Magn Reson Imaging. 2010; 31:430–439. [PubMed: 20099357]
53. Mercuri E, Pichiecchio A, Allsop J, Messina S, Pane M, Muntoni F. Muscle MRI in inherited neuromuscular disorders: past, present, and future. J Magn Reson Imaging. 2007; 25:433–440. [PubMed: 17260395]
54. Garrood P, Hollingsworth KG, Eagle M, Aribisala BS, Birchall D, Bushby K, Straub V. MR imaging in Duchenne muscular dystrophy: quantification of T1-weighted signal, contrast uptake, and the effects of exercise. J Magn Reson Imaging. 2009; 30:1130–1138. [PubMed: 19856446]
55. Straub V, Pierre G, Mercuri E. TREAT-NMD workshop: pattern recognition in genetic muscle diseases using muscle MRI. Neuromuscul Disord. 2012; 22(Suppl 2):S42–S53. [PubMed: 22980768]
56. Huang Y, Majumdar S, Genant HK, Chan WP, Sharma KR, Yu P, Mynhier M, Miller RG. Quantitative MR relaxometry study of muscle composition and function in Duchenne muscular dystrophy. J Magn Reson Imaging. 1994; 4:59–64. [PubMed: 8148557]
57. Phoenix J, Betal D, Roberts N, Helliwell TR, Edwards RH. Objective quantification of muscle and fat in human dystrophic muscle by magnetic resonance image analysis. Muscle Nerve. 1996; 19:302–310. [PubMed: 8606693]
58. Kan HE, Scheenen TW, Wohlgemuth M, Klomp DW, van Loosbroek-Wagenmans I, Padberg GW, Heerschap A. Quantitative MR imaging of individual muscle involvement in facioscapulohumeral muscular dystrophy. Neuromuscul Disord. 2009; 19:357–362. [PubMed: 19329315]
59. Friedman SD, Poliachik SL, Carter GT, Budech CB, Bird TD, Shaw DW. The magnetic resonance imaging spectrum of facioscapulohumeral muscular dystrophy. Muscle Nerve. 2012; 45:500–506. [PubMed: 22431082]
60. Strobel K, van den Hoff J, Pietzsch J. Localized proton magnetic resonance spectroscopy of lipids in adipose tissue at high spatial resolution in mice in vivo. J Lipid Res. 2008; 49:473–480. [PubMed: 18024705]
61. Hamilton G, Yokoo T, Bydder M, Cruite I, Schroeder ME, Sirlin CB, Middleton MS. In vivo characterization of the liver fat 1H MR spectrum. NMR Biomed. 2011; 24:784–790. [PubMed: 21834002]
62. Berglund J, Ahlström H, Kullberg J. Model-based mapping of fat unsaturation and chain length by chemical shift imaging-phantom validation and in vivo feasibility. Magn Reson Med. 2012; 68:1815–1827. [PubMed: 22334300]
63. Petersen P, Måsson S. Simultaneous quantification of fat content and fatty acid composition using MR imaging. Magn Reson Med. 2013; 69:688–697. [PubMed: 22532403]

64. Sharma P, Martin DR, Pineda N, Xu Q, Vos M, Anania F, Hu X. Quantitative analysis of T2-correction in single-voxel magnetic resonance spectroscopy of hepatic lipid fraction. J Magn Reson Imaging. 2009; 29:629–635. [PubMed: 19243059]
65. McGavock JM, Lingvay I, Zib I, Tillery T, Salas N, Unger R, Levine BD, Raskin P, Victor RG, Szczepaniak LS. Cardiac steatosis in diabetes mellitus: a 1H-magnetic resonance spectroscopy study. Circulation. 2007; 116:1170–1175. [PubMed: 17698735]
66. Lingvay I, Esser V, Legendre JL, Price AL, Wertz KM, Adams-Huet B, Zhang S, Unger RH, Szczepaniak LS. Noninvasive quantification of pancreatic fat in humans. J Clin Endocrinol Metab. 2009; 94:4070–4076. [PubMed: 19773401]
67. Krssak M, Petersen KF, Dresner A, DiPietro L, Vogel SM, Rothman DL, Shulman GI, Roden M. Intramyocellular lipid concentrations are correlated with insulin sensitivity in humans: a 1H NMR spectroscopy study. Diabetologia. 1999; 42:113–116. [PubMed: 10027589]
68. Sinha R, Dufour S, Petersen KF, LeBon V, Enoksson S, Ma YZ, Savoye M, Rothman DL, Shulman GI, Caprio S. Assessment of skeletal muscle triglyceride content by 1H nuclear magnetic resonance spectroscopy in lean and obese adolescents: relationships to insulin sensitivity, total body fat, and central adiposity. Diabetes. 2002; 51:1022–1027. [PubMed: 11916921]
69. Boesch C, Machann J, Vermathen P, Schick F. Role of proton MR for the study of muscle lipid metabolism. NMR Biomed. 2006; 19:968–988. [PubMed: 17075965]
70. Weis J, Johansson L, Ortiz-Nieto F, Ahlström H. Assessment of lipids in skeletal muscle by high-resolution spectroscopic imaging using fat as the internal standard: Comparison with water referenced spectroscopy. Magn Reson Med. 2008; 59:1259–1265. [PubMed: 18421681]
71. Fischer MA, Nanz D, Shimakawa A, Schirmer T, Guggenberger R, Chhabra A, Carrino JA, Andreisek G. Quantification of muscle fat in patients with low back pain: comparison of multi-echo MR imaging with single-voxel MR spectroscopy. Radiology. 2013; 256:555–563. [PubMed: 23143025]
72. Pansini V, Monnet A, Salleron J, Hardouin P, Cortet B, Cotten A. 3 Tesla 1H MR spectroscopy of hip bone marrow in a healthy population, assessment of normal fat content values and influence of age and sex. J Magn Reson Imaging. 2013 DOI: 10.100/jmri.24176.
73. Karampinos DC, Melkus G, Baum T, Bauer JS, Rummeny EJ, Krug R. Bone marrow fat quantification in the presence of trabecular bone: initial comparison between water-fat imaging and single-voxel MRS. Magn Reson Med. 2013 DOI: 10.1002/mrm.24775.
74. Månsson S, Peterson P, Johansson E. Quantification of low fat contents: a comparison of MR imaging and spectroscopy methods at 1.5 and 3T. Magn Reson Imaging. 2012; 30:1461–1467. [PubMed: 22835942]
75. Lunati E, Farace P, Nicolato E, Righetti C, Marzola P, Sbarbati A, Osculati F. Polyunsaturated fatty acids mapping by 1H MR-chemical shift imaging. Magn Reson Med. 2001; 46:879–883. [PubMed: 11675638]
76. Ren J, Dimitrov I, Sherry AD, Malloy CR. Composition of adipose tissue and marrow fat in humans by 1H NMR at 7 Tesla. J Lipid Res. 2008; 49:2055–2062. [PubMed: 18509197]
77. Naressi A, Couturier C, Castang I, de Beer R, Graveron-Demilly D. Java-based graphical user interface for MRUI, a software package for quantitation of in vivo/medical magnetic resonance spectroscopy signals. Comput Biol Med. 2001; 31:269–286. [PubMed: 11334636]
78. Provencher SW. Automatic quantitation of localized in vivo 1H spectra with LCModel. NMR Biomed. 2001; 14:260–264. [PubMed: 11410943]
79. Bydder M, Hamilton G, Yokoo T, Sirlin CB. Optimal phased-array combination for spectroscopy. Magn Reson Imaging. 2008; 26:847–850. [PubMed: 18486392]
80. An L, Willem van der Veen J, Li S, Thomasson DM, Shen J. Combination of multichannel single-voxel MRS signals using generalized least squares. J Magn Reson Imaging. 2013; 37:1445–1450. [PubMed: 23172656]
81. Felblinger J, Jung B, Slotboom J, Boesch C, Kreis R. Methods and reproducibility of cardiac/respiratory double-triggered (1)H-MR spectroscopy of the human heart. Magn Reson Med. 1999; 42:903–910. [PubMed: 10542349]

82. Schär M, Kozerke S, Boesiger P. Navigator gating and volume tracking for double-triggered cardiac proton spectroscopy at 3 Tesla. Magn Reson Med. 2004; 51:1091–1095. [PubMed: 15170826]
83. Frahm J, Bruhn H, Gyngell ML, Merboldt KD, Hanicke W, Sauter R. Localized high-resolution proton NMR spectroscopy using stimulated echoes: initial applications to human brain in vivo. Magn Reson Med. 1989; 9:79–93. [PubMed: 2540396]
84. Bottomley PA. Spatial localization in NMR spectroscopy in vivo. Ann N Y Acad Sci. 1987; 508:333–348. [PubMed: 3326459]
85. Goelman G, Liu S, Fleyscher R, Fleysher L, Grossman RI, Gonen O. Chemical-shift artifact reduction in hadamard-encoded MR spectroscopic imaging at high (3T and 7T) magnetic fields. Magn Reson Med. 2007; 58:167–173. [PubMed: 17659608]
86. Scheenen TW, Klomp DW, Wijnen JP, Heerschap A. Short echo time 1H-MRSI of the human brain at 3T with minimal chemical shift displacement errors using adiabatic refocusing pulses. Magn Reson Med. 2008; 59:1–6. [PubMed: 17969076]
87. Fuchs A, Luttje M, Boesiger P, Henning A. SPECIAL semi-LASER with lipid artifact compensation for 1H MRS at 7T. Magn Reson Med. 2013; 69:603–612. [PubMed: 22517487]
88. Hu HH, Kim HW, Nayak KS, Goran MI. Comparison of fat-water MRI and single-voxel MRS in the assessment of hepatic and pancreatic fat fractions in humans. Obesity (Silver Spring). 2010; 18:841–847. [PubMed: 19834463]
89. Boesch C, Kreis R. Observation of intramyocellular lipids by 1H-magnetic resonance spectroscopy. Ann N Y Acad Sci. 2000; 904:25–31. [PubMed: 10865706]
90. Posse S, Otazo R, Dager SR, Alger J. MR spectroscopic imaging: principles and recent advances. J Magn Reson Imaging. 2013; 37:1301–1325. [PubMed: 23188775]
91. Lin FH, Tsai SY, Otazo R, Caprihan A, Wald LL, Belliveau JW, Posse S. Sensitivity-encoded (SENSE) proton echo-planar spectroscopic imaging (PEPSI) in the human brain. Magn Reson Med. 2007; 57:249–257. [PubMed: 17260356]
92. Larson PEZ, Hu S, Lustig M, Kerr AB, Nelson SJ, Kurhanewicz J, Pauly JM, Vigneron DB. Fast dynamic 3D MR spectroscopic imaging with compressed sensing and multiband excitation pulses for hyperpolarized 13C studies. Magn Reson Med. 2011; 65:610–619. [PubMed: 20939089]
93. Furuyama JK, Wilson NE, Burns BL, Nagarajan R, Margolis DJ, Thomas MA. Application of compressed sensing to multidimensional spectroscopic imaging in human prostate. Magn Reson Med. 2012; 67:1499–1505. [PubMed: 22505247]
94. Mareci TH, Brooker HR. Essential considerations for spectral localization using indirect gradient encoding of spatial information. J Magn Reson. 1991; 92:229–246.
95. Le Roux P, Gilles RJ, McKinnon GC, Carlier PG. Optimized outer volume suppression for single-shot fast spin-echo cardiac imaging. J Magn Reson Imaging. 1998; 8:1022–1032. [PubMed: 9786138]
96. Scheenen TW, Klomp DW, Roll SA, Futterer JJ, Barentsz JO, Heerschap A. Fast acquisition-weighted three-dimensional proton MR spectroscopic imaging of the human prostate. Magn Reson Med. 2004; 52:80–88. [PubMed: 15236370]
97. Schick F, Eismann B, Jung WI, Bongers H, Bunse M, Lutz O. Comparison of localized proton NMR signals of skeletal muscle and fat tissue in vivo: two lipid compartments in muscle tissue. Magn Reson Med. 1993; 29:158–167. [PubMed: 8429779]
98. Boesch C. Musculoskeletal spectroscopy. J Magn Reson Imaging. 2007; 25:321–338. [PubMed: 17260389]
99. Khuu A, Ren J, Dimitrov I, Woessner D, Murdoch J, Sherry AD, Malloy CR. Orientation of lipid strands in the extracellular compartment of muscle: effect on quantitation of intramyocellular lipids. Magn Reson Med. 2009; 61:16–21. [PubMed: 19097207]
100. Ren J, Sherry AD, Malloy CR. 1H MRS of intramyocellular lipids in soleus muscle at 7 T: spectral simplification by using long echo times without water suppression. Magn Reson Med. 2010; 64:662–671. [PubMed: 20578068]
101. Ortiz-Nieto F, Johansson L, Ahlström H, Weis J. Quantification of lipids in human lower limbs using yellow bone marrow as the internal reference: gender-related effects. J Magn Reson Imaging. 2010; 28:676–682.

102. Schrauwen-Hinderling VB, van Loon LJ, Koopman R, Nicolay K, Saris WH, Kooi ME. Intramyocellular lipid content is increased after exercise in nonexercising human skeletal muscle. J Appl Physiol. 2003; 95:2328–2332. [PubMed: 12923116]
103. Bachmann OP, Dahl DB, Brechtel K, Machann J, Haap M, Maier T, Loviscach M, Stumvoll M, Claussen CD, Schick F, Häring HU, Jacob S. Effects of intravenous and dietary lipid challenge on intramyocellular lipid content and the relation with insulin sensitivity in humans. Diabetes. 2001; 50:2579–2584. [PubMed: 11679437]
104. Zehnder M, Christ ER, Ith M, Acheson KJ, Pouteau E, Kreis R, Trepp R, Diem P, Boesch C, Décombaz J. Intramyocellular lipid stores increase markedly in athletes after 1.5 days lipid supplementation and are utilized during exercise in proportion to their content. Eur J Appl Physiol. 2006; 98:341–354. [PubMed: 16902796]
105. Jonkers RA, Geraedts TR, van Loon LJ, Nicolay K, Prompers JJ. Multitissue assessment of in vivo postprandial intracellular lipid partitioning in rats using localized 1H-[13C] magnetic resonance spectroscopy. Magn Reson Med. 2012; 68:997–1006. [PubMed: 22213012]
106. Goodpaster BH, He J, Watkins S, Kelley DE. Skeletal muscle lipid content and insulin resistance: evidence for a paradox in endurance-trained athletes. J Clin Endocrinol Metab. 2001; 86:5755–5761. [PubMed: 11739435]
107. Wijsman CA, van Opstal AM, Kan HE, Maier AB, Westendorp RG, Slagboom PE, Webb AG, Mooijaart SP, van Heemst D. Proton magnetic resonance spectroscopy shows lower intramyocellular lipid accumulation in middle-aged subjects predisposed to familial longevitiy. Am J Physiol Endocrinol Metab. 2012; 302:E344–E348. [PubMed: 22094471]
108. Décombaz J, Schmitt B, Ith M, Decarli B, Diem P, Kreis R, Hoppeler H, Boesch C. Postexercise fat intake repletes intramyocellular lipids but no faster in trained than in sedentary subjects. Am J Physiol Regul Integr Comp Physiol. 2001; 281:R760–R769. [PubMed: 11506990]
109. Haase A, Frahm J, Hånicke W, Matthaei D. 1H NMR chemical shift selective (CHESS) imaging. Phys. Med. Biol. 1985; 30:341–344. [PubMed: 4001160]
110. Meyer CH, Pauly JM, Makovski A, Nishimura DG. Simultaneous spatial and spectral selective excitation. Magn Reson Med. 1990; 15:287–304. [PubMed: 2392053]
111. Kaldoudi E, Williams SC, Barker GJ, Tofts PS. A chemical shift selective inversion recovery sequence for fat-suppressed MRI: theory and experimental validation. Magn Reson Imaging. 1993; 11:341–355. [PubMed: 8505868]
112. Block W, Pauly JM, Kerr A, Nishimura DG. Consistent fat suppression with compensated spectral-spatial pulses. Magn Reson Med. 1997; 38:198–206. [PubMed: 9256098]
113. Schick F. Simultaneous highly selective MR water and fat imaging using a simple new type of spectral-spatial excitation. Magn Reson Med. 1998; 40:194–202. [PubMed: 9702701]
114. Laurent WM, Bonny JM, Renou JP. Imaging of water and fat fractions in high-field MRI with multiple slice chemical shift-selective inversion recovery. J Magn Reson Imaging. 2000; 12:488–496. [PubMed: 10992317]
115. Machann J, Bachmann OP, Brechtel K, Dahl DB, Wietek B, Klumpp B, Häring HU, Claussen CD, Jacob S, Schick F. Lipid content in the musculature of the lower leg assessed by fat selective MRI: intra- and interindividual differences and correlation with anthropometric and metabolic data. J Magn Reson Imaging. 2003; 17:350–357. [PubMed: 12594726]
116. Peng Q, McColl RW, Wang J, Chia JM, Weatherall PT. Water-saturated three-dimensional balanced steady-state free precession for fast abdominal fat quantification. J Magn Reson Imaging. 2005; 21:263–271. [PubMed: 15723372]
117. Makrogiannis S, Serai S, Fishbein KW, Schreiber C, Ferrucci L, Spencer RG. Automated quantification of muscle and fat in the thigh from water-, fat-, and nonsuppressed MR images. J Magn Reson Imaging. 2012; 35:1152–1161. [PubMed: 22170747]
118. Machann J, Thamer C, Schnoedt B, Stefan N, Häring HU, Claussen CD, Fritsche A, Schick F. Hepatic lipid accumulation in healthy subjects: a comparative study using spectral fat-selective MRI and volume-localized 1H-MR spectroscopy. Magn Reson Med. 2006; 55:913–917. [PubMed: 16506186]
119. Schwenzer NF, Machann J, Martirosian P, Stefan N, Schraml C, Fritsche A, Claussen CD, Schick F. Quantification of pancreatic lipomatosis and liver steatosis by MRI: comparison of in/

opposed-phase and spectral-spatial excitation techniques. Invest Radiol. 2008; 43:330–337. [PubMed: 18424954]

120. Raschpichler MC, Sorge I, Hirsch W, Mende M, Sergeyev E, Kruber D, Koerner A, Schick F. Evaluating childhood obesity: magnetic resonance-based quantification of abdominal adipose tissue and liver fat in children. Rofo. 2012; 184:324–332. [PubMed: 22322443]
121. Delfaut EM, Beltran J, Johnson G, Rousseau J, Marchandise X, Cotton A. Fat suppression in MR imaging: techniques and pitfalls. Radiographics. 1999; 19:373–382. [PubMed: 10194785]
122. Ma J. Dixon techniques for water and fat imaging. J Magn Reson Imaging. 2008; 28:543–558. [PubMed: 18777528]
123. Bley TA, Wieben O, Francois CJ, Brittain JH, Reeder SB. Fat and water magnetic resonance imaging. J Magn Reson Imaging. 2010; 31:4–18. [PubMed: 20027567]
124. An L, Xiang QS. Chemical shift imaging with spectrum modeling. Magn Reson Med. 2001; 46:126–130. [PubMed: 11443718]
125. Yu H, McKenzie CA, Brodsky E, Brittain JH, Reeder SB. Multiecho water-fat separation and simultaneous R2* estimation with multifrequency fat spectrum modeling. Magn Reson Med. 2008; 60:1122–1134. [PubMed: 18956464]
126. Dixon WT. Simple proton spectroscopic imaging. Radiology. 1984; 153:189–194. [PubMed: 6089263]
127. Sepponen RE, Sipponen JT, Tanttu JI. A method for chemical shift imaging: demonstration of bone marrow involvement with proton chemical shift imaging. J Comput Assist Tomogr. 1984; 8:585–587. [PubMed: 6330183]
128. Blatter DD, Morris AH, Ailion DC, Cutillo AG, Case TA. Asymmetric spin echo sequences. A simple new method for obtaining NMR 1H spectral images. Invest Radiol. 1985; 20:845–853. [PubMed: 4077438]
129. Cassidy FH, Yokoo T, Aganovic L, Hanna RF, Bydder M, Middleton MS, Hamilton G, Chavez AD, Schwimmer JB, Sirlin CB. Fatty liver disease: MR imaging techniques for the detection and quantification of liver steatosis. Radiographics. 2009; 29:231–260. [PubMed: 19168847]
130. Hussain HK, Chenevert TL, Londy FJ, Gulani V, Swanson SD, McKenna BJ, Appelman HD, Adusumilli S, Greenson JK, Conjeevaram HS. Hepatic fat fraction: MR imaging for quantitative measurement and display--early experience. Radiology. 2005; 237:1048–1055. [PubMed: 16237138]
131. Börnert P, Keupp J, Eggers H, Aldefeld B. Whole-body 3D water/fat resolved continuously moving table imaging. J Magn Reson Imaging. 2007; 25:660–665. [PubMed: 17326078]
132. Berglund J, Johansson L, Ahlström H, Kullberg J. Three-point Dixon method enables whole-body water and fat imaging of obese subjects. Magn Reson Med. 2010; 63:1659–1668. [PubMed: 20512869]
133. Boll DT, Marin D, Redmon GM, Zink SI, Merkle EM. Pilot study assessing differentiation of steatosis hepatis, hepatic iron overload, and combined disease using two-point Dixon MRI at 3 T: in vitro and in vivo results of a 2D decomposition technique. Am J Roentgenol. 2010; 194:964–971. [PubMed: 20308498]
134. Gloor M, Fasler S, Fischmann A, Haas T, Bieri O, Heinimann K, Wetzel SG, Scheffler K, Fischer D. Quantification of fat infiltration in oculopharyngeal muscular dystrophy: comparison of three MR imaging methods. J Magn Reson Imaging. 2011; 33:203–210. [PubMed: 21182140]
135. Gaeta M, Messina S, Mileto A, Vita GL, Ascenti G, Vinci S, Bottari A, Vita G, Settineri N, Bruschetta D, Racchiusa S, Minutoli F. Muscle fat-fraction and mapping in Duchenne muscular dystrophy: evaluation of disease distribution and correlation with clinical assessments: Preliminary experience. Skeletal Radiol. 2012; 41:955–961. [PubMed: 22069033]
136. Hollingsworth KG, de Sousa PL, Straub V, Carlier PG. Towards harmonization of protocols for MRI outcome measures in skeletal muscle studies: consensus recommendations from two TREAT-NMD NMR workshops, 2 May 2010, Stockholm, Sweden, 1-2 October 2009, Paris, France. Neuromuscul Disord. 2012; 22(Suppl 2):S54–S67. [PubMed: 22980769]
137. Karampinos DC, Baum T, Nardo L, Alizai H, Yu H, Carballido-Gamio J, Yap SP, Shimakawa A, Link TM, Majumdar S. Characterization of the regional distribution of skeletal muscle adipose

tissue in type 2 diabetes using chemical shift-based water/fat separation. J Magn Reson Imaging. 2012; 35:899–907. [PubMed: 22127958]

138. Poonawalla AH, Sjoberg BP, Rehm JL, Hernando D, Hines CD, Irarrazaval P, Reeder SB. Adipose tissue MRI for quantitative measurement of central obesity. J Magn Reson Imaging. 2013; 37:707–716. [PubMed: 23055365]
139. Wokke BH, Bos C, Reijnierse M, van Rijswijk CS, Eggers H, Webb A, Verschuuren JJ, Kan HE. Comparison of Dixon and T1-weighted MR methods to assess the degree of fat infiltration in Duchenne muscular dystrophy patients. J Magn Reson Imaging. 2013 DOI: 10.1002/jmri.23998.
140. Karampinos DC, Melkus G, Baum T, Bauer JS, Rummeny EJ, Krug R. Bone marrow fat quantification in the presence of trabecular bone: initial comparison between water-fat imaging and single-voxel MRS. Magn Reson Med. 2013 DOI: 10.1002/mrm.24775.
141. Eggers H, Brendel B, Duijndam A, Herigault G. Dual-echo Dixon imaging with flexible choice of echo times. Magn Reson Med. 2011; 65:96–107. [PubMed: 20860006]
142. Berglund J, Ahlström H, Johansson L, Kullberg J. Two-point Dixon method with flexible echo times. Magn Reson Med. 2011; 65:994–1004. [PubMed: 21413063]
143. Hernando D, Kellman P, Haldar JP, Liang ZP. Robust water/fat separation in the presence of large field inhomogeneities using a graph cut algorithm. Magn Reson Med. 2010; 63:79–90. [PubMed: 19859956]
144. Berglund J, Kullberg J. Three-dimensional water/fat separation and T2* estimation based on whole-image optimization--application in breathhold liver imaging at 1.5 T. Magn Reson Med. 2012; 67:1684–1693. [PubMed: 22189760]
145. Tsao J, Jiang Y. Hierarchical IDEAL: Fast, robust, and multiresolution separation of multiple chemical species from multiple echo times. Magn Reson Med. 2013; 70:155–159. [PubMed: 22887356]
146. Hernando D, Liang ZP, Kellman P. Chemical shift-based water/fat separation: a comparison of signal models. Magn Reson Med. 2010; 64:811–822. [PubMed: 20593375]
147. Karampinos DC, Yu H, Shimakawa A, Link TM, Majumdar S. Chemical shift-based water/fat separation in the presence of susceptibility-induced fat resonance shift. Magn Reson Med. 2012; 68:1495–1505. [PubMed: 22247024]
148. Peterson P, Månsson S. Fat quantification using multi-echo sequences with bipolar gradients: investigation of accuracy and noise performance. Magn Reson Med. 2013 DOI: 10.1002/mrm.24657.
149. Horng DE, Hernando D, Hines CD, Reeder SB. Comparison of R2* correction methods for accurate fat quantification in fatty liver. J Magn Reson Imaging. 2013; 37:414–422. [PubMed: 23165934]
150. Wood JC, Enriquez C, Ghugre N, Tyzka JM, Carson S, Nelson MD, Coates TD. MRI R2 and R2* mapping accurately estimates hepatic iron concentration in transfusion-dependent thalassemia and sickle cell disease patients. Blood. 2005; 106:1460–1465. [PubMed: 15860670]
151. Storey P, Thompson AA, Carqueville CL, Wood JC, de Freitas RA, Rigsby CK. R2* imaging of transfusional iron burden at 3T and comparison with 1.5T. J Magn Reson Imaging. 2007; 25:540–547. [PubMed: 17326089]
152. Taylor BA, Loeffler RB, Song R, McCarville MB, Hankins JS, Hillenbrand CM. Simultaneous field and R2* mapping to quantify liver iron content using autoregressive moving average modeling. J Magn Reson Imaging. 2012; 35:1125–1132. [PubMed: 22180325]
153. Hernando D, Kramer JH, Reeder SB. Multipeak fat-corrected complex R2* relaxometry: theory, optimization and clinical validation. Magn Reson Med. 2013 DOI: 10.1002/mrm.24593.
154. Hines CD, Frydrychowicz A, Hamilton G, Tudorascu DL, Vigen KK, Yu H, McKenzie CA, Sirlin CB, Brittain JH, Reeder SB. T1 independent, T2* corrected chemical shift based fat-water separation with multi-peak fat spectral modeling is an accurate and precise measure of hepatic steatosis. J Magn Reson Imaging. 2011; 33:873–881. [PubMed: 21448952]
155. Meisamy S, Hines CD, Hamilton G, Sirlin CB, McKenzie CA, Yu H, Brittain JH, Reeder SB. Quantification of hepatic steatosis with T1-independent, T2-corrected MR imaging with spectral modeling of fat: blinded comparison with MR spectroscopy. Radiology. 2011; 258:767–775. [PubMed: 21248233]

156. Tang A, Tan J, Sun M, Hamilton G, Bydder M, Wolfson T, Gamst AC, Middleton M, Brunt EM, Loomba R, Lavine JE, Schwimmer JB, Sirlin CB. Nonalcoholic fatty liver disease: MR imaging of liver proton density fat fraction to assess hepatic steatosis. Radiology. 2013; 267:422–431. [PubMed: 23382291]

157. Liu CY, McKenzie CA, Yu H, Brittain JH, Reeder SB. Fat quantification with IDEAL gradient echo imaging: correction of bias from T1 and noise. Magn Reson Med. 2007; 58:354–364. [PubMed: 17654578]

158. Bydder M, Yokoo T, Hamilton G, Middleton MS, Chavez AD, Schwimmer JB, Lavine JE, Sirlin CB. Relaxation effects in the quantification of fat using gradient echo imaging. Magn Reson Imaging. 2008; 26:347–359. [PubMed: 18093781]

159. Reeder SB, Hu HH, Sirlin CB. Proton density fat-fraction: A standardized MR-based biomarker of issue fat concentration. J Magn Reson Imaging. 2012; 36:1011–1014. [PubMed: 22777847]

160. Mashhood A, Railkar R, Yokoo T, Levin Y, Clark L, Fox-Bosetti S, Middleton MS, Riek J, Kauh E, Dardzinski BJ, Williams D, Sirlin C, Shire NJ. Reproducibility of hepatic fat fraction measurement by magnetic resonance imaging. J Magn Reson Imaging. 2013; 37:1359–1370. [PubMed: 23172799]

161. Frontini A, Cinti S. Distribution and development of brown adipocytes in the murine and human adipose organ. Cell Metab. 2010; 11:253–256. [PubMed: 20374956]

162. Ravussin E, Galgani JE. The implication of brown adipose tissue for humans. Annu Rev Nutr. 2011; 31:33–47. [PubMed: 21548774]

163. Wronska A, Kmiec Z. Structural and biochemical characteristics of various white adipose tissue depots. Acta Physiol (Oxf). 2012; 205:194–208. [PubMed: 22226221]

164. Nedergaard J, Bengtsson T, Cannon B. Three years with adult human brown adipose tissue. Ann N Y Acad Sci. 2010; 1212:E20–36. [PubMed: 21375707]

165. Lee P, Swarbrick MM, Ho KK. Brown adipose tissue in adult humans: a metabolic renaissance. Endocr Rev. 2013; 34:413–438. [PubMed: 23550082]

166. Ouellet V, Labbe SM, Blondin DP, Phoenix S, Guerin B, Haman F, Turcotte EE, Richard D, Carpentier AC. Brown adipose tissue oxidative metabolism contributes to energy expenditure during acute cold exposure in humans. J Clin Invest. 2012; 122:545–552. [PubMed: 22269323]

167. Muzik O, Mangner TJ, Leonard WR, Kumar A, Janisse J, Granneman JG. 15O PET measurement of blood flow and oxygen consumption in cold-activated human brown fat. J Nucl Med. 2013; 54:523–531. [PubMed: 23362317]

168. Cannon B, Nedergaard J. Brown adipose tissue: function and physiological significance. Physiol Rev. 2004; 84:277–359. [PubMed: 14715917]

169. Cinti S. The role of brown adipose tissue in human obesity. Nutr Metab Cardiovasc Dis. 2006; 16:569–574. [PubMed: 17113764]

170. Aherne W, Hull D. Brown adipose tissue and heat production in the newborn infant. J Pathol Bacteriol. 1996; 91:223–234. [PubMed: 5941392]

171. Heaton JM. The distribution of brown adipose tissue in the human. J Anat. 1972; 112:35–39. [PubMed: 5086212]

172. Merklin RJ. Growth and distribution of human fetal brown fat. Anat Rec. 1974; 178:637–645. [PubMed: 4856126]

173. Mortola JP, Merazzi D, Naso L. Blood flow to the brown adipose tissue of conscious young rabbits during hypoxia in cold and warm conditions. Pflugers Arch. 1999; 437:225–260.

174. Da Motta AC, Tunkel DE, Westra WH, Yousem DM. Imaging findings of a hibernoma of the neck. Am J Neuroradiol. 2006; 27:1658–1659. [PubMed: 16971608]

175. Mavrogenis AF, Coll-Mesa L, Drago G, Gambarotti M, Ruggieri P. Hibernomas: clinicopathological features, diagnosis, and treatment of 17 cases. Orthopedics. 2011; 34:e755–e759. [PubMed: 22049958]

176. Kumar R, Deaver MT, Czemiak BA, Madwell JE. Intraosseous hibernoma. Skeletal Radiol. 2011; 40:641–645. [PubMed: 21207023]

177. Papathanassiou ZG, Alberghini M, Taieb S, Errani C, Picci P, Vanel D. Imaging of hibernomas: a retrospective study on twelve cases. Clin Sarcoma Res. 2011 DOI: 10.1186/2045-3329-1-3.

178. Elqatni M, Ghafir D. Hibernoma of the neck. N Eng J Med. 2012; 367:1636.
179. Dundamadappa SK, Shankar S, Danrad R, Singh A, Vijayaraghavan G, Kim Y, Perugini R. Imaging of brown fat associated with adrenal pheochromocytoma. Acta Radiol. 2007; 48:468–472. [PubMed: 17453531]
180. Carter BW, Schucany WG. Brown adipose tissue in a newborn. Proc (Bayl Univ Med Cent). 2008; 21:328–330. [PubMed: 18628932]
181. Osculati F, Leclercq F, Sbarbati A, Zancanaro C, Cinti S, Antonakis K. Morphological identification of brown adipose tissue by magnetic resonance imaging in the rat. Eur J Radiol. 1989; 9:112–114. [PubMed: 2743984]
182. Osculati F, Sbarbati A, Leclercq F, Zancanaro C, Accordini C, Antonakis K, Boicelli A, Cinti S. The correlation between magnetic resonance imaging and ultrastructral patterns of brown adipose tissue. J Submicrosc Cytol Pathol. 1991; 23:167–174. [PubMed: 2036625]
183. Sbarbati A, Baldassarri AM, Zancanaro C, Boicelli A, Osculati F. In vivo morphometry and functional morphology of brown adipose tissue by magnetic resonance imaging. Anat Rec. 1991; 231:293–297. [PubMed: 1763812]
184. Chen YI, Cypess AM, Sass CA, Brownell AL, Jokivarsi KT, Kahn CR, Kwong KK. Anatomical and functional assessment of brown adipose tissue by magnetic resonance imaging. Obesity (Silver Spring). 2012; 20:1519–1526. [PubMed: 22343821]
185. Hamilton G, Smith DL Jr. Bydder M, Nayak KS, Hu HH. MR properties of brown and white adipose tissues. J Magn Reson Imaging. 2011; 34:468–473. [PubMed: 21780237]
186. Zancanaro C, Nano R, Marchioro C, Sbarbati A, Boicelli A, Osculati F. Magnetic resonance spectroscopy investigations of brown adipose tissue and isolated brown adipocytes. J Lipid Res. 1994; 35:2191–2199. [PubMed: 7897317]
187. Sbarbati A, Guerrini U, Marzola P, Asperio R, Osculati F. Chemical shift imaging at 4.7 Tesla of brown adipose tissue. J Lipid Res. 1997; 38:343–347. [PubMed: 9162753]
188. Lunati E, Marzola P, Nicolato E, Fedrigo M, Villa M, Sbarbati A. In vivo quantitative lipidic map of brown adipose tissue by chemical shift imaging at 4.7 Tesla. J Lipid Res. 1999; 40:1395–1400. [PubMed: 10428975]
189. Peng XG, Ju S, Fang F, Wang Y, Fang K, Cui X, Liu G, Li P, Mao H, Teng GJ. Comparison of brown and white adipose tissue fat fractions in ob, seipin and Fsp27 gene knockout mice by chemical shift selective imaging and 1H MR spectroscopy. Am J Physiol Endocrinol Metab. 2013; 304:E160–167. [PubMed: 23149622]
190. Hu HH, Smith DL Jr. Nayak KS, Goran MI, Nagy TR. Identification of brown adipose tissue in mice with fat-water IDEAL-MRI. J Magn Reson Imaging. 2010; 31:1195–1202. [PubMed: 20432356]
191. Hu HH, Hines CD, Smith DL Jr. Reeder SB. Variations in T2* and fat content of murine brown and white adipose tissues by chemical-shift MRI. Magn Reson Imaging. 2012; 30:323–329. [PubMed: 22244539]
192. Smith DL, Yang Y, Hu HH, Zhai G, Nagy TR. Measurement of interscapular brown adipose tissue of mice in differentially housed temperatures by chemical-shift-encoded water-fat magnetic resonance imaging. J Magn Reson Imaging. 2013 DOI: 10.1002/jmri.24138.
193. Holstila M, Virtanen KA, Grönroos TV, Laine J, Lepomäki V, Saunavaara J, Lisinen I, Komu M, Hannukainen H, Nuutila P, Parkkola R, Borra RJH. Measurement of brown adipose tissue mass using a novel dual-echo magnetic resonance imaging approach: a validation study. Metabolism. 2013 DOI: 10.1016/j.metabol.2013.03.002.
194. Hu HH, Tovar JP, Pavlova Z, Smith ML, Gilsanz V. Unequivocal identification of brown adipose tissue in a human infant. J Magn Reson Imaging. 2012; 35:938–942. [PubMed: 22180228]
195. Hu HH, Perkins TG, Chia JM, Gilsanz V. Characterization of human brown adipose tissue by chemical-shift water-fat MRI. Am J Roentgenology. 2013; 200:177–183.
196. Hu HH, Yin L, Aggabao PC, Perkins TG, Chia JM, Gilsanz V. Comparison of brown and white adipose tissues in infants and children with chemical-shift-encoded water-fat MRI. J Magn Reson Imaging. 2013 DOI: 10.1002/jmri.24053.
197. Lidell ME, Betz MJ, Dahlqvist Leinhard O, Heglind M, Elander L, Slawik M, Mussack T, Nilsson D, Romu T, Nuutila P, Virtanen KA, Beuschlein F, Persson A, Borga M, Enerbäck S.

Evidence of two types of brown adipose tissue in humans. Nat Med. 2013; 19:631–634. [PubMed: 23603813]

198. Gifford A, Kullberg J, Berglund J, Towse TF, Walker RC, Avison MJ, Welch EB. Detection of brown adipose tissue in an adult human using fat-water MRI with validation by cold-activated PET. Proceedings of the International Society for Magnetic Resonance in Medicine. 2013; 21:1520.
199. Wayte SC, Reddy NL, Jones TA, Adesanya O, Yoe YC, Randeva HS, Kumar S, Hutchinson CE, Barber TM. Identification of brown adipose tissue using Dixon imaging in a human adult with histological confirmation. Proceedings of the International Society for Magnetic Resonance in Medicine. 2013; 21:4052.
200. Lundström E, Berglund J, Johansson L, Bergsten P, Ahlström H, Kullberg J. Water-fat imaging of supraclavcular brown and white adipose tissue at 1.5T: initial results in healthy volunteers. Proceedings of the International Society for Magnetic Resonance in Medicine. 2013; 21:4050.
201. van Rooijen BD, van der Lans AA, Brans B, Wildberger JE, Mootaghy FM, Schrauwen P, Backes WH, van Marken Lichtenbelt WD. Imaging cold-activated brown adipose tissue using dynamic T2*-weighted magnetic resonance imaging and 2-deoxy-2-[18F]fluoro-D-glucose positrion emission tomography. Invest Radiol. 2013 [epub ahead of print].
202. Branca RT, Warren WS. In vivo brown adipose tissue detection and characterization using water-lipid intermolecular zero-quantum coherences. Magn Reson Med. 2011; 65:313–319. [PubMed: 20939093]
203. Bao J, Cui X, Zheng Z, Cai C, Chen Z. Mapping brown adipose tissue through intermolecular double-quantum magnetic resonance imaging at 7 Tesla. Proceedings of the International Society for Magnetic Resonance in Medicine. 2012; 20:381.
204. Hu HH, Nagy TR, Li Y, Goran MI, Nayak KS. Quantification of absolute fat mass by magnetic resonance imaging: a validation study against chemical assay. International Journal of Body Composition Research. 2011; 9:111–122. [PubMed: 23204926]
205. Joshi AA, Hu HH, Goran MI, Leahy RM, Nayak KS. Automatic intra-subject registration-based segmentation of abdominal fat from 3D water-fat MRI. J Magn Reson Imaging. 2013; 37:423–430. [PubMed: 23011805]
206. Thörmer G, Bertram HH, Garnov N, Peter V, Schütz T, SHang E, Büher M, Kahn T, Busse H. Software for automated MRI-based quantification of abdominal fat and preliminary evaluation in morbidly obese patients. J Magn Reson Imaging. 2013; 37:1140–1150.
207. Brunner G, Nambia V, Yang E, Kumar A, Virani SS, Kougias P, Shah D, Lumsden A, Ballantyne CM, Morrisett JD. Automatic quantification of muscle volumes in magnetic resonance imaging scans of the lower extremities. Magn Reson Imaging. 2011; 29:1065–1075. [PubMed: 21855242]
208. Commean PK, Tuttle LJ, Hastings MK, Strube MJ, Mueller MJ. Magnetic resonance imaging measurement reproducibility for calf muscle and adipose tissue volume. J Magn Reson Imaging. 2011; 34:1285–1294. [PubMed: 21964677]
209. Hiba B, Richard N, Hébert LJ, Coté C, Nejjari M, Vial C, Bouhour F, Puymirat J, Janier M. Quantitative assessment of skeletal muscle degeneration in patients with myotonic dystrophy type 1 using MRI. J Magn Reson Imaging. 2012; 35:678–685. [PubMed: 22069222]
210. Valentinitsch A, Karampinos DC, Alizai H, Subburaj K, Kumar D, Link TM, Majumdar S. Automated unsupervised multi-parametric classification of adipose tissue depots in skeletal muscle. J Magn Reson Imaging. 2013; 37:917–927. [PubMed: 23097409]
211. Sinha S, SInha U, Edgerton VR. In vivo diffusion tensor imaging of the human calf muscle. J Magn Reson Imaging. 2006; 24:182–190. [PubMed: 16729262]
212. Williams SE, Heemskerk AM, Welch EB, Li K, Damon BM, Park JH. Quantitative effects of inclusion of fat on muscle diffusion tensor MRI measurements. J Magn Reson Imaging. 2013 DOI: 10.1002/jmri.24045.
213. Walker GE, Verti B, Marzullo P, Savia G, Mencarelli M, Zurleni F, Liuzzi A, Di Blasio AM. Deep subcutaneous adipose tissue: a distinct abdominal adipose depot. Obesity (Silver Spring). 2007; 15:1933–1943. [PubMed: 17712110]

214. Kelley DE, Thaete FL, Troost F, Huwe T, Goodpaster BH. Subdivisions of subcutaneous abdominal adipose tissue and insulin resistance. Am J Physiol Endocrinol Metab. 2000; 278:E941–948. [PubMed: 10780952]

215. Lundbom J, Hakkarainen A, Lundbom N, Taskinen MR. Deep subcutaneous adipose tissue is more saturated than superficial subcutaneous adipose tissue. Int J Obes (Lond). 2013; 37:620–622. [PubMed: 22641063]

216. Machann J, Schleicher E, Würslin C, Fritsche A, Schick F. Intra- and interindividual differences in fatty acid composition at various locations of the body assessed by ^{1}H-MRS. Proceedings of the International Society for Magnetic Resonance in Medicine. 2013; 21:1511.

217. Bydder M, Girard O, Hamilton G. Mapping the double bonds in triglycerides. Magn Reson Imaging. 2011; 29:1041–1046. [PubMed: 21868182]

218. Pou KM, Massaro JM, Hoffmann U, Vasan RS, Maurovich-Horvat P, Larson MG, Keaney JF Jr. Meigs JB, Lipinska I, Kathiresan S, Murabito JM, O'Donnell CJ, Benjamin EJ, Fox CS. Visceral and subcutaneous adipose tissue volumes are cross-sectionally related to markers of inflammation and oxidative stress: the Framingham Heart Study. Circulation. 2007; 116:1234–1241. [PubMed: 17709633]

219. Tchoukalova YD, Koutsari C, Karpyak MV, Votruba SB, Wendland E, Jensen MD. Subcutaneous adipocyte size and body fat distribution. Am J Clin Nutr. 2008; 87:56–63. [PubMed: 18175737]

220. Spalding KL, Arner E, Westermark PO, Bernard S, Buchholz BA, Bergmann O, Blomqvist L, Hoffstedt J, Näslund E, Britton T, Concha H, Hassan M, Rydén M, Frisén J, Arner P. Dynamics of fat cell turnover in humans. Nature. 2008; 453:783–787. [PubMed: 18454136]

221. Weyer C, Foley JE, Bogardus C, Tataranni PA, Pratley RE. Enlarged subcutaneous abdominal adipocyte size, but not obesity itself, predicts type II diabetes independent of insulin resistance. Diabetologia. 2000; 43:1498–1506. [PubMed: 11151758]

222. Kabir M, Stefanovski D, Hsu IR, Iyer M, Woolcott OO, Zheng D, Catalano KJ, Chiu JD, Kim SP, Harrison LN, Ionut V, Lottati M, Bergman RN, Richey JM. Large size cells in the visceral adipose depot predict insulin resistance in the canine model. Obesity (Silver Spring). 2011; 19:2121–2129. [PubMed: 21836643]

223. Khurana A, Nejadnik H, Gawande R, Lin G, Lee S, Messing S, Castaneda R, Derugin N, Pisani L, Lue TF, Daldrup-Link HE. Intravenous Ferumoxytol allows noninvasive MR imaging monitoring of macrophage migration into stem cell transplants. Radiology. 2012; 264:803–811. [PubMed: 22820731]

224. Brandejsky V, Kreis R, Boesch C. Restricted or severly hindered diffusion in intramyocellular lipids in human skeletal muscle shown by in vivo proton MR spectroscopy. Magn Reson Med. 2012; 67:310–316. [PubMed: 21674617]

225. Steidle G, Eibofner F, Schick F. Quantitative diffusion imaging of adipose tissue in the human lower leg at 1.5 T. Magn Reson Med. 2011; 65:1118–1124. [PubMed: 21413077]

226. Rothman, Dl; De Feyter, Hm; de Graaf, RA.; Mason, GF.; Behar, KL. 13C MRS studies of neuroenergetics and neurotransmitter cycling in humans. NMR Biomed. 2011; 24:943–957. [PubMed: 21882281]

227. Sbarbati A, Cavallini I, Marzola P, Nicolato E, Osculati F. Contrast-enhanced MRI of brown adipose tissue after pharmacological stimulation. Magn Reson Med. 2006; 55:715–718. [PubMed: 16506160]

228. Khanna A, Branca RT. Detecting brown adipose tissue activity with BOLD MRI in mice. Magn Reson Med. 2012; 68:1285–1290. [PubMed: 22231619]

229. Soher BJ, Wyatt C, Reeder SB, MacFall JR. Noninvasive temperature mapping with MRI using chemical shift water-fat separation. Magn Reson Med. 2010; 63:1238–1246. [PubMed: 20432295]

230. Lau AZ, Chen AP, Gu Y, Ladouceur-Wodzak M, Nayak KS, Cunningham CH. Noninvasive identification and assessment of functional brown adipose tissue in rodents using hyperpolarized 13C imaging. Int J Obes (Lond). 2013 DOI: 10.1038/ijo.2013.58.

231. Friesen-Waldner LJ, Wade TP, Wiens CN, Thind K, Harris JK, Sinclair KJ, McCurdy CM, Chen AP, Borradaile NM, McKenzie C. Hyperpolarised [1-^{13}C]-pyruvate metabolism in brown fat. Proceedings of the International Society for Magnetic Resonance in Medicine. 2013; 21:3912.

232. Branca RT, White C, Zhang L. Detection of brown fat mass and activity by hyperpolarized xenon MR. Proceedings of the International Society for Magnetic Resonance in Medicine. 2013; 21:404.

233. Branca RT, Zhang L, White C, He T. Detection of brown fat thermogenesis by hyperpolarized Xenon gas MR. Proceedings of the International Society for Magnetic Resonance in Medicine. 2013; 21:814.

234. Waldén TB, Hansen IR, Timmons JA, Cannon B, Nedergaard J. Recruited vs. nonrecruited molecular signatures of brown, “brite,” and white adipose tissues. Am J Physiol Endocrinol Metab. 2012; 302:E19–31. [PubMed: 21828341]

235. Cypess AM, White AP, Vernochet C, Schultz TJ, Xue R, Sass CA, Huang TL, Roberts-Toler C, Weiner LS, Sze C, Chacko AT, Deschamps LN, Herder LM, Truchan N, Glasgow AL, Holman AR, Gavrila A, Hasselgren PO, Mori MA, Molla M, Tseng YH. Anatomical localization, gene expression profiling and functional characterization of adult human neck brown fat. Nat Med. 2013; 19:635–639. [PubMed: 23603815]

236. Kelly DP. Irisin, light my fire. Science. 2012; 336:42–43. [PubMed: 22491843]

237. Nakamura K, Morrison SF. Central efferent pathways mediating skin cooling-evoked sympathetic thermogenesis in brown adipose tissue. Am J Physiol Regul Integr Comp Physiol. 2007; 292:R127–136. [PubMed: 16931649]

238. Endo T, Kobayashi T. Thyroid-stimulating hormone receptor in brown adipose tissue is involved in the regulation of thermogenesis. Am J Physiol Endocrinol Metab. 2008; 295:E514–E518. [PubMed: 18559984]

239. Ichimiya H, Arakawa S, Sato T, Shimada T, Chiba M, Soma Y, Mizoguchi M, Tomonari K, Iwasaka H, Hatano Y, Okamoto O, Fujiwara S. Involvement of brown adipose tissue in subcutaneous fat necrosis of the newborn. Dermatology. 2011; 223:207–210. [PubMed: 21968020]

240. van der Veen DR, Shao J, Chapman S, Leevy WM, Duffield GE. A diurnal rhythm in glucose uptake in brown adipose tissue revealed by in vivo PET-FDG imaging. Obesity (Silver Spring). 2012; 20:1527–1529. [PubMed: 22447290]

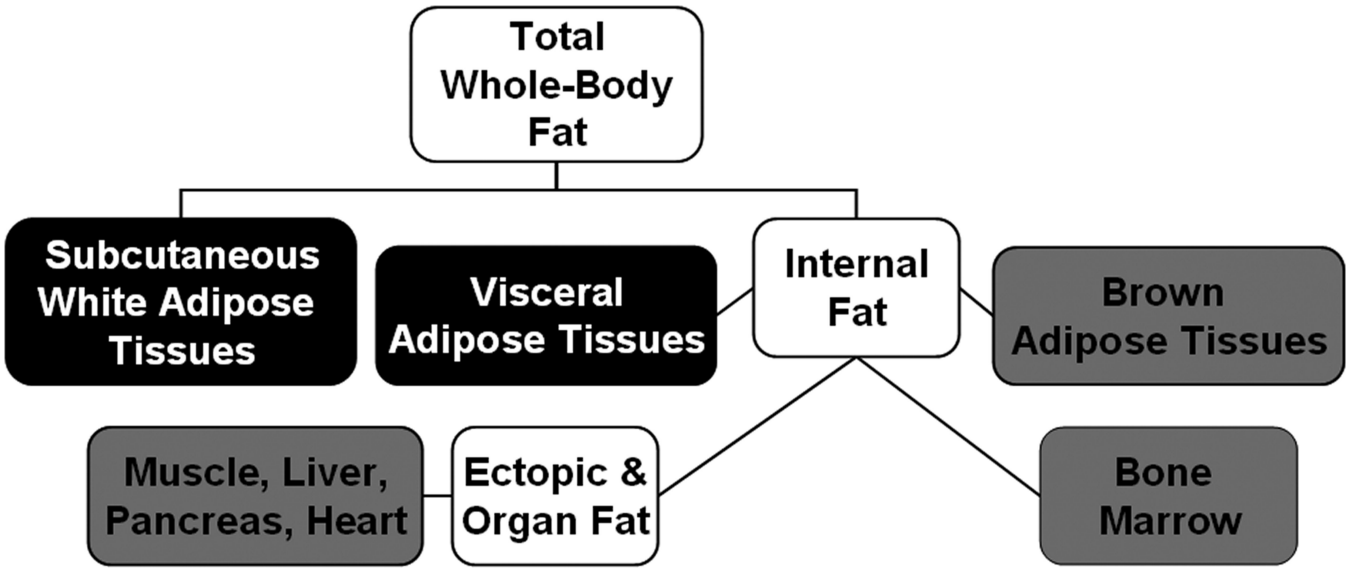

Figure 1.

Classification of body fat locations commonly quantified by MR and reported in literature. Elements in black are white adipose tissue depots, and are typically quantified in units of volume (ml, L) or subsequently converted to mass (g, kg). They are measured via imaging pulse sequences. Grey elements are locations where fat exists diffusely and heterogeneously, whether naturally or abnormally. The typical quantitative endpoint here is a percent fat content, which can be derived with MR imaging and spectroscopy pulse sequences. One common measure is the fat-signal fraction (e.g. the ratio of fat signal to the sum of water and fat signals). Spectroscopy can also be used to characterize triglyceride properties at all locations, yielding information such as chain length and unsaturation levels.

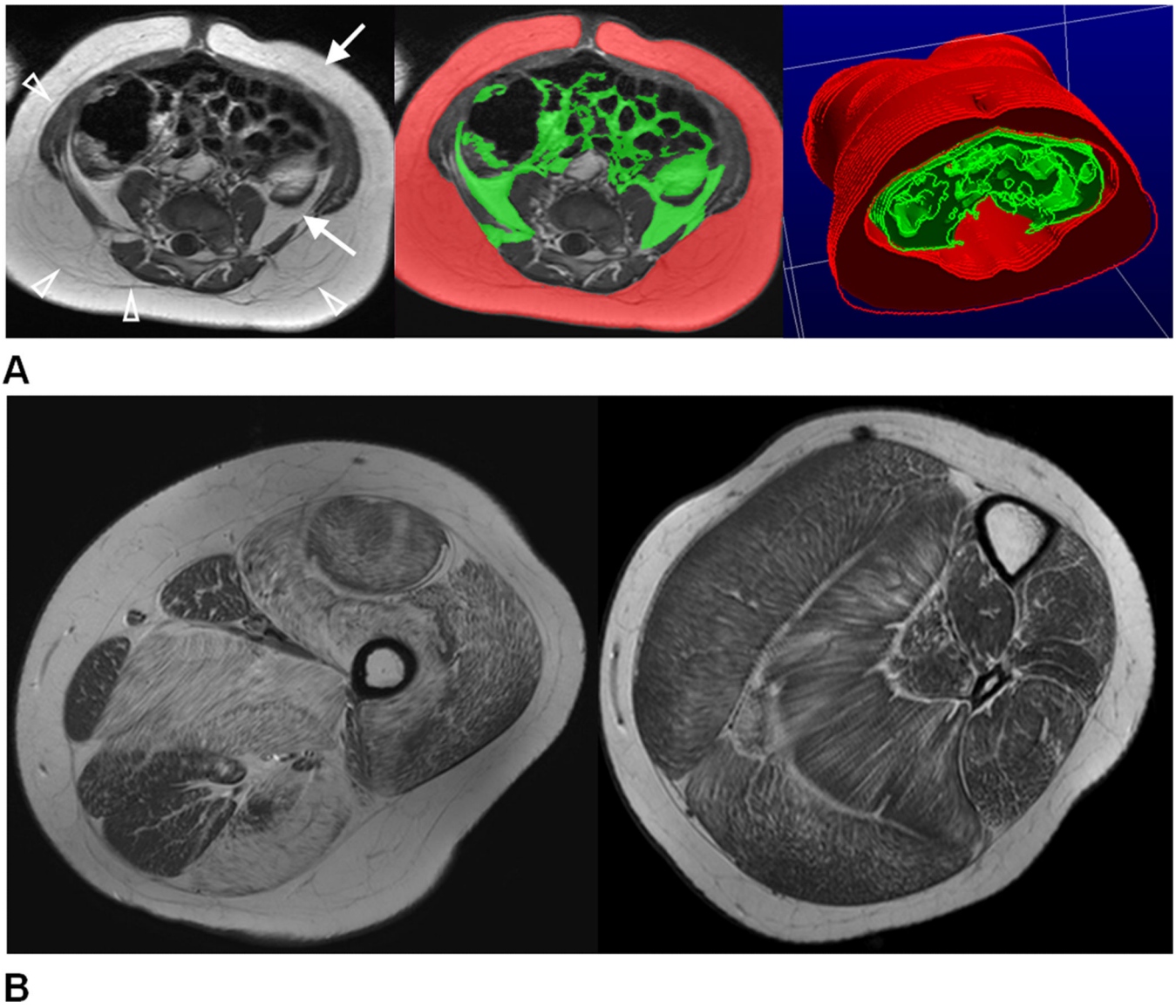

Figure 2.

(A) An example of axial T_1-weighted image in the abdomen. Higher signal intensities of adipose tissue (arrows) in contrast to darker muscles and organs can be clearly seen. Arrowheads denote the thin fascia that divides the deep and superficial subcutaneous adipose tissue layers. The native data from these scans are typically contiguous multi-slice or three-dimensional with high spatial resolution, permitting post-processing and rendering procedures to further visualize subcutaneous (red) and visceral (green) distributions. Illustration courtesy of Wei Shen, M.D., St. Luke-Roosevelt Hospital and Columbia University, using sliceOmatic (Tomovision, Inc.) software. **(B)** Axial T_1-weighted images in the upper and lower left leg of a 9-year-old boy with Duchenne muscular dystrophy. Fatty subcutaneous and bone marrow adipose tissues are characterized by high signal intensities. The varying degrees and patterns of fat accumulation within the skeletal muscles are clearly evident.

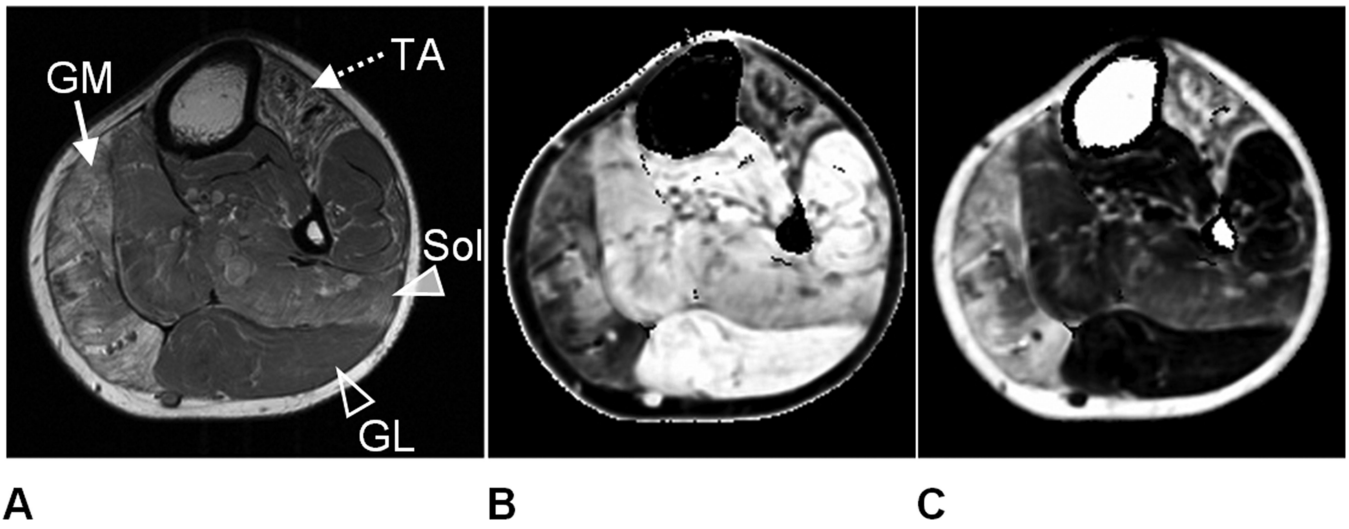

Figure 3.

Lower extremity left leg images of a patient with facioscapulohumeral dystrophy. In **(A)**, a T_1-weighted image is shown for anatomical reference. Note the evident heterogeneous fatty accumulation within the gastrocnemius medial (GM - solid arrow) and tibialis anterior (TA - dotted arrow) muscles. Multi-echo T_2-mapping was used to generate **(B)** water and **(C)** fat component images. Note the clear separation and proper assignment of subcutaneous and bone marrow adipose tissue to the fat image. In both images, muscles significantly affected by fat (GM, TA) are strongly contrasted from less-fat-involved muscles (gastrocnemius lateral (GL) – open arrowhead, soleus (Sol) – solid arrowhead). A ratio between **(B)** and **(C)** can yield a fat-signal fraction map of the imaging slice for quantitative analysis.

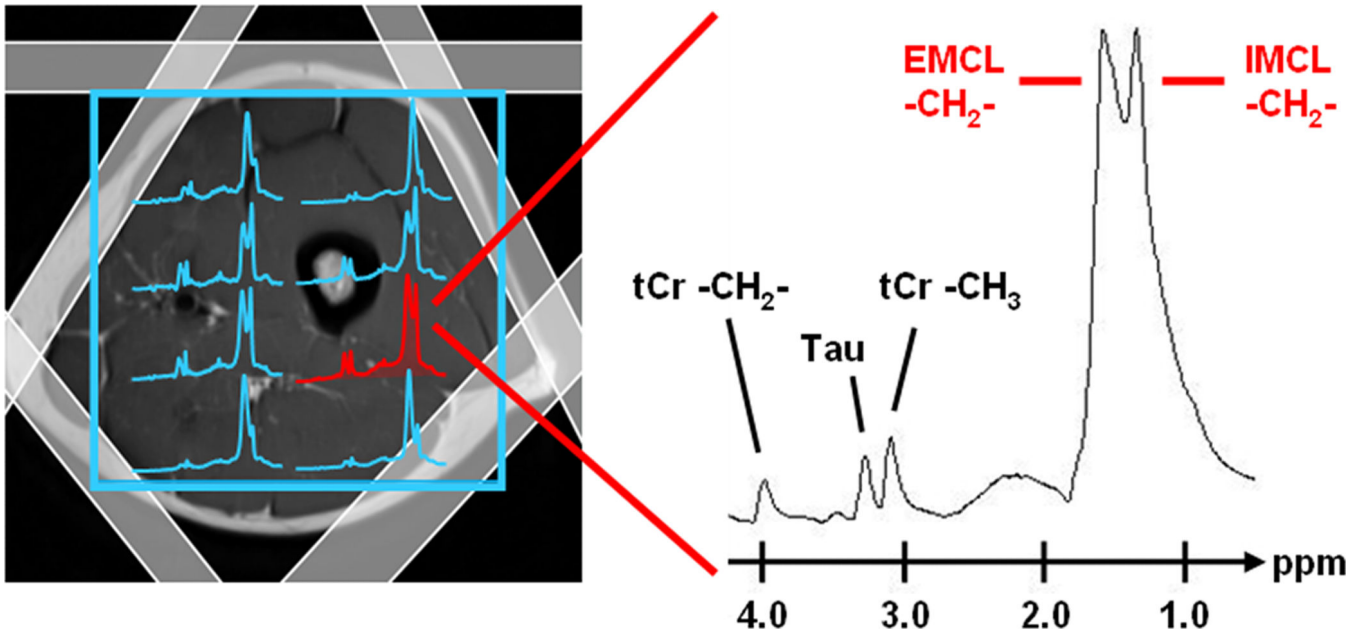

Figure 4.

An example of 2D proton chemical shift imaging for characterization of intra- (IMCL) and extramyocellular (EMCL) lipids in lower extremity skeletal muscles is illustrated. Prior to data acquisition from the volume-of-interest (blue grid outline), signals from subcutaneous adipose tissue are suppressed using outer volume suppression bands (shaded white rectangles). Note the differences in spectral separation between IMCL and EMCL methylene resonances, along with tCr – creatine and Tau – taurine. Illustration courtesy of Peter Vermathen, Ph.D., University Bern, Switzerland.

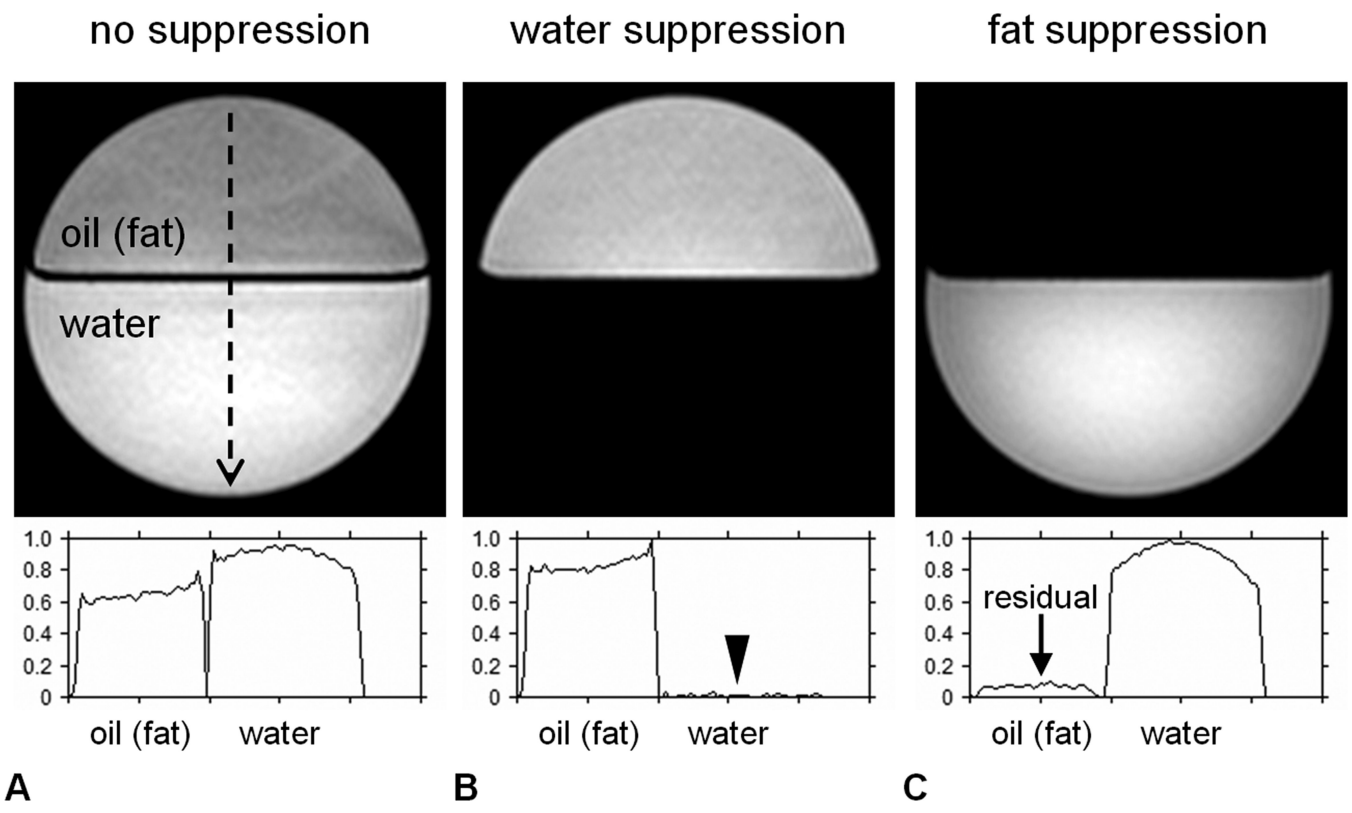

Figure 5.

Demonstration of frequency-selective MRI in a bilayer water-oil phantom **(A)** with no RF suppression, **(B)** with RF suppression spectrally targeted on the water resonance, and **(C)** with RF suppression spectrally targeted on the methylene resonance of fat. All three images were acquired with otherwise same imaging parameters and system settings and are illustrated using the same grayscale window/level display. A vertical signal profile line is plotted from top to bottom along each image (black dashed line) and shown in the accompanying plots. In **(B)**, water suppression has effectively saturated all water signals (black arrowhead). In **(C)**, residual fat signals (arrow) remain in the oil compartment. This is because the oil contains unsaturated TG (e.g. olefinic protons, vinyl groups) and only proton signals from the methylene peak of fat have been selectively suppressed. Image ratios of **(A-C)** can yield methylene fat-signal fraction and water-signal fraction maps.

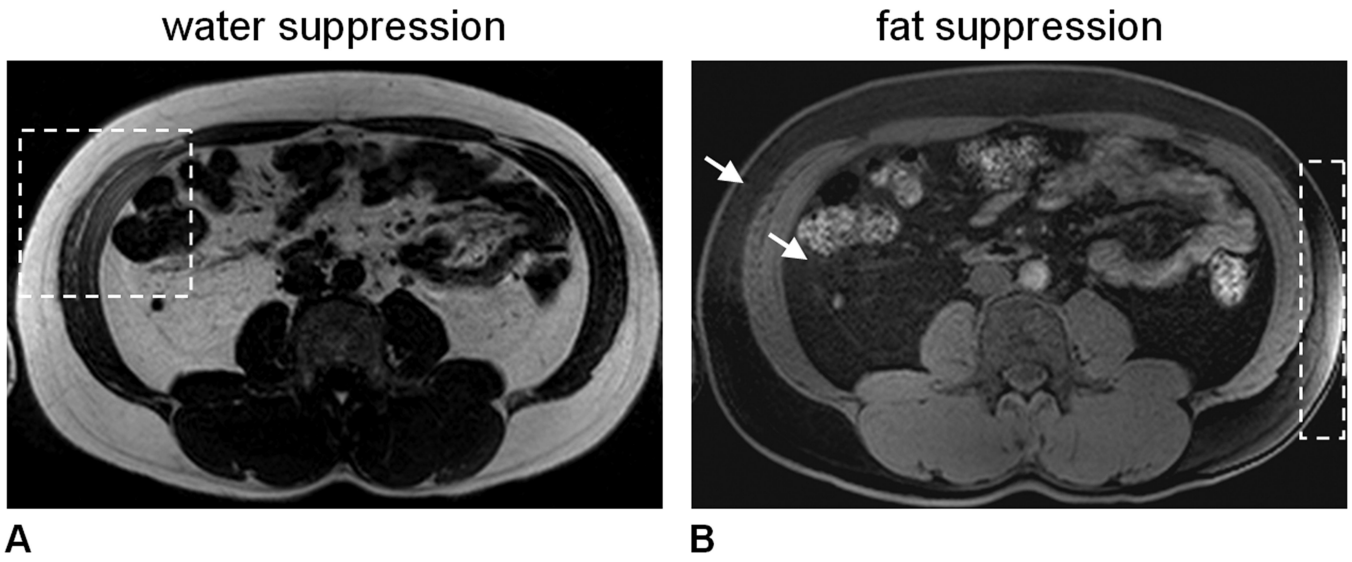

Figure 6.

Frequency-selective MRI, demonstrated in the form of **(A)** water-suppression and **(B)** fat-suppression in the same subject at 3.0 Tesla. Good overall suppression is achieved, except in areas outlined by dashed boxes. In the water-suppressed image **(A)**, the right oblique and transversus abdominis muscles show appreciable signal intensity. Conversely in the fat-suppressed image **(B)**, subcutaneous adipose tissue within the dashed box has noticeable signal intensity. The poor local suppression performance is due to spatially varying B0 magnetic field inhomogeneity. Similar to Figure 5, note in **(B)** that the subcutaneous and visceral adipose tissue depots are not completely suppressed and exhibit residual signals (arrows).

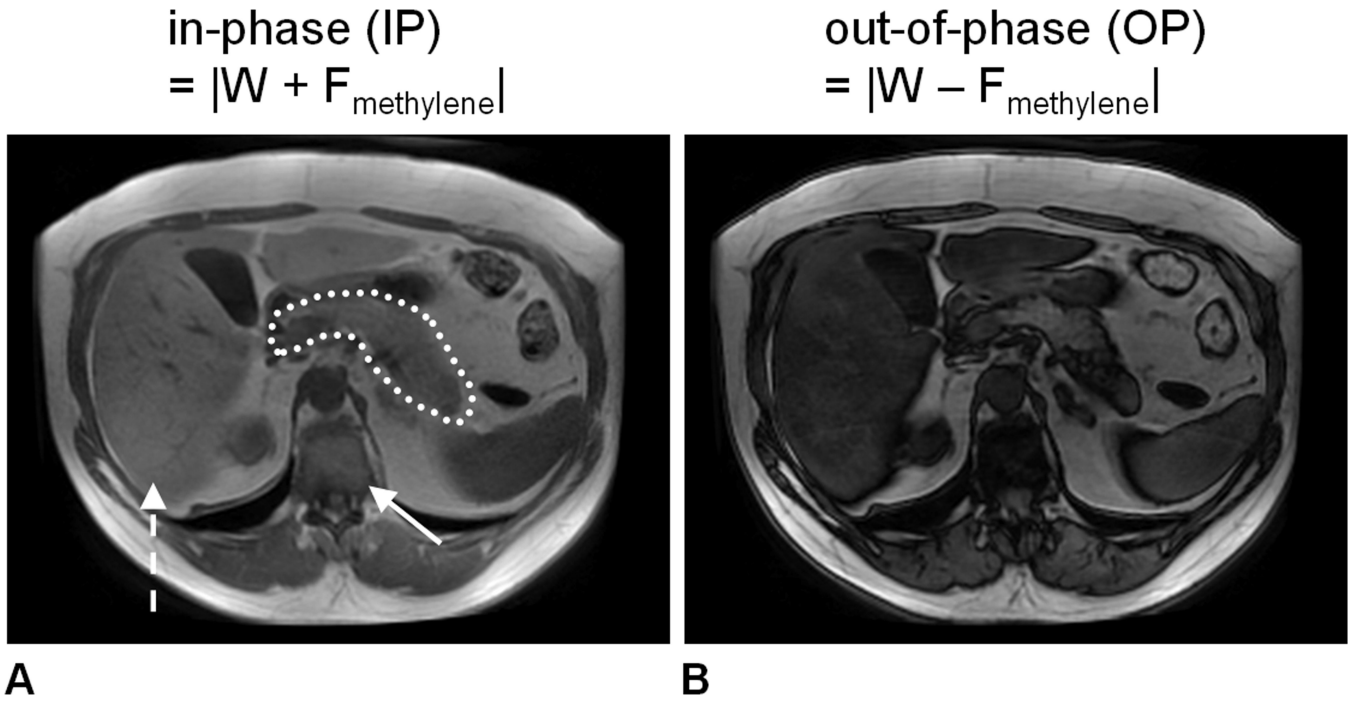

Figure 7.

An example of the two two-point Dixon technique, demonstrated in a subject with known non-alcoholic fatty liver disease (24% hepatic fat-signal fraction previously determined by spectroscopy). Two sets of images are acquired in a single scan with water and methylene fat signals **(A)** in-phase (IP) and **(B)** out-of-phase (OP). Note that the liver signal intensity (dashed arrow) in the OP image is markedly darker than in the IP image, indicative of possible steatosis. Similar signal variations can be observed in the pancreas (dotted tracing) and to a lesser extent in the muscles. Note that IP and OP signal variations are not observed in the subcutaneous and visceral adipose tissues (fat-dominant). For comparison, note also the vertebral bone marrow (arrow), which contains near equal amounts of water and fat. This leads to a near complete cancellation of water and fat signals in the OP image.

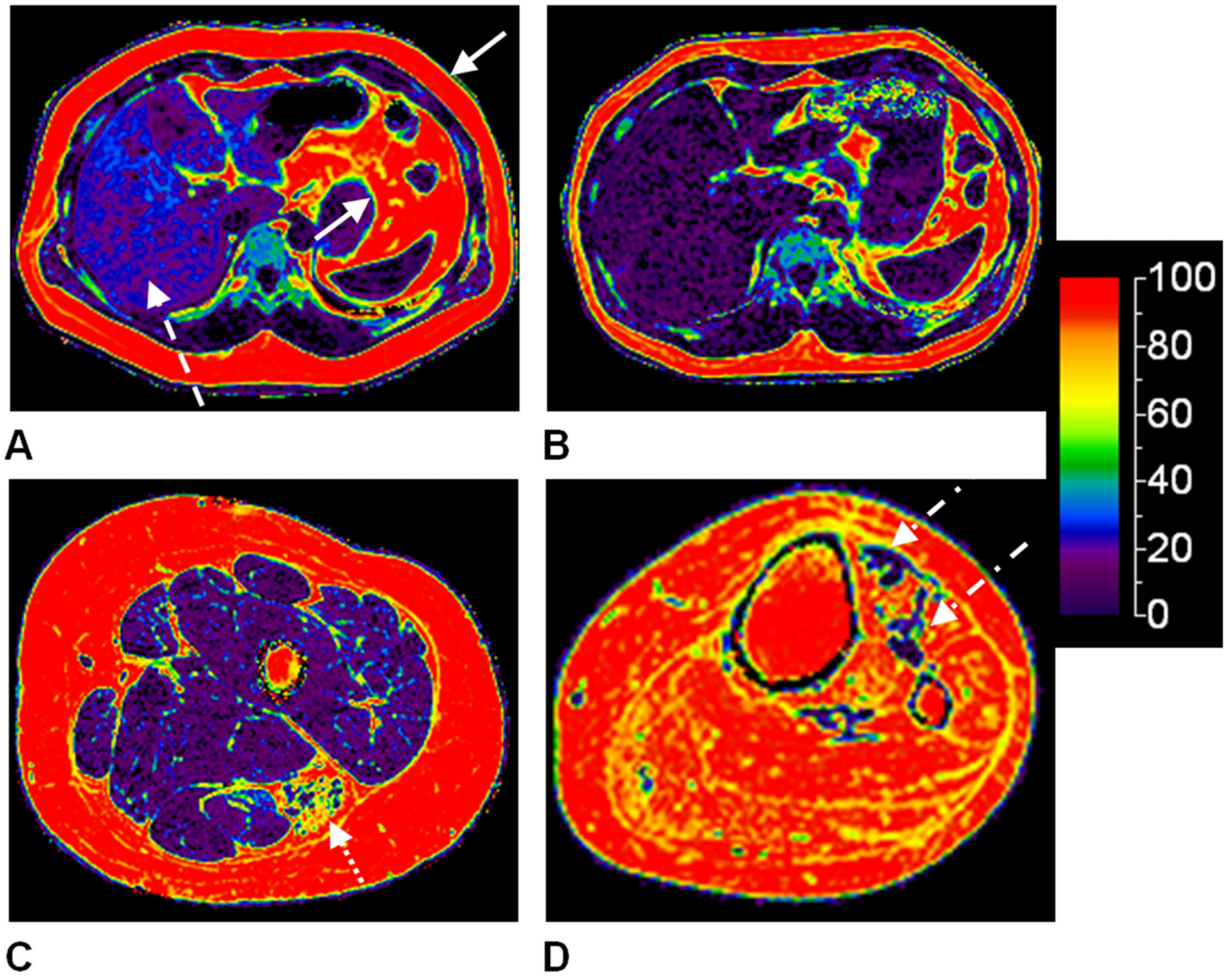

Figure 8.

Examples of proton-density fat fraction maps from multi-echo water-fat MRI are shown in color on a full scale of 0-100%. An adult male, 43 years of age, **(A)** before and **(B)** after a 10-month self-initiated diet and exercise regimen is illustrated. The decrease in liver fat content (dashed arrow) and subcutaneous and visceral adipose tissue (mostly omental) volumes (solid arrows) is evident. The liver fat fraction in **(A)** was approximately 22%; in **(B)**, it has reduced to approximately 6%. The two data sets were acquired on a 3.0 Tesla Signa HDx system from GE Healthcare. Representative axial images of the left thigh and calf from **(C)** an 11-year-old male and **(D)** an 11-year-old female with spina bifida (myelomeningocele), respectively, are shown. In **(C)**, preferential fat accumulation in the biceps femoris muscle (dotted arrow) of the hamstrings is evident. In **(D)**, almost all calf muscles show complete fat infiltration, and only the tibialis anterior muscle exhibits some remaining muscle tissues (dot-dash arrows). Leg data was acquired on a 3.0 Telsa Achieva system from Philips Healthcare.

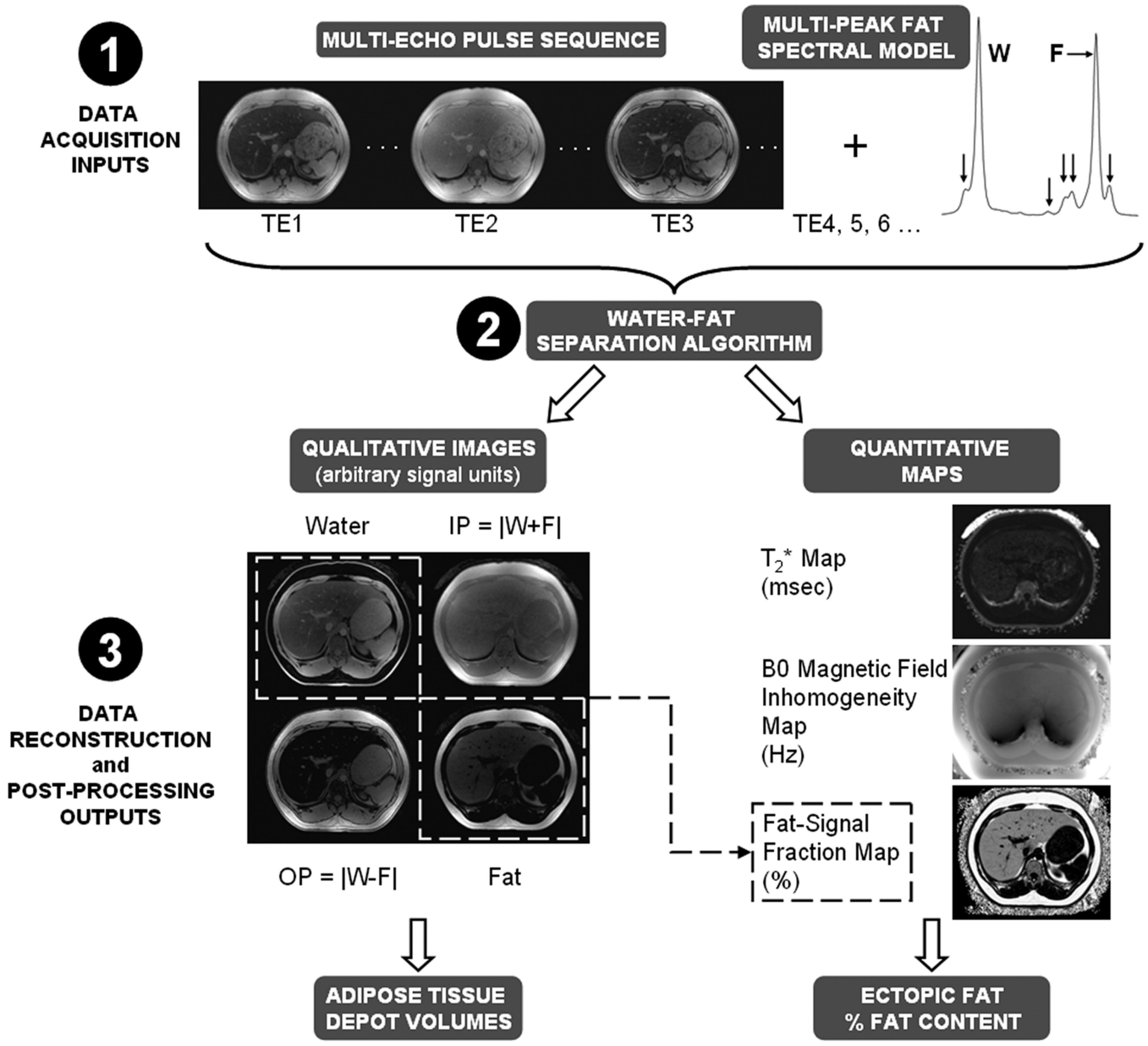

Figure 9.

A general schematic of multi-echo WFI. (Step 1) Data acquisition occurs at several echo times. (Step 2) Utilizing a multi-peak spectral model for fat (horizontal arrow: major methylene peak; vertical arrows: additional minor resonances), a reconstruction algorithm, often iterative, yields a set of co-registered grayscale water, fat, in-phase (IP), and out-of-phase (OP) volumes. (Step 3) In parallel, co-registered quantitative maps for T_2* relaxation, B0 magnetic field inhomogeneity, and fat-signal fraction are generated. When noise and relaxometry effects are accounted for, the fat-signal fraction closely approximates the true underlying proton-density fat fraction. The seven outputs provide avenues for computing adipose tissue depot volumes and percent fat content in ectopic sites.

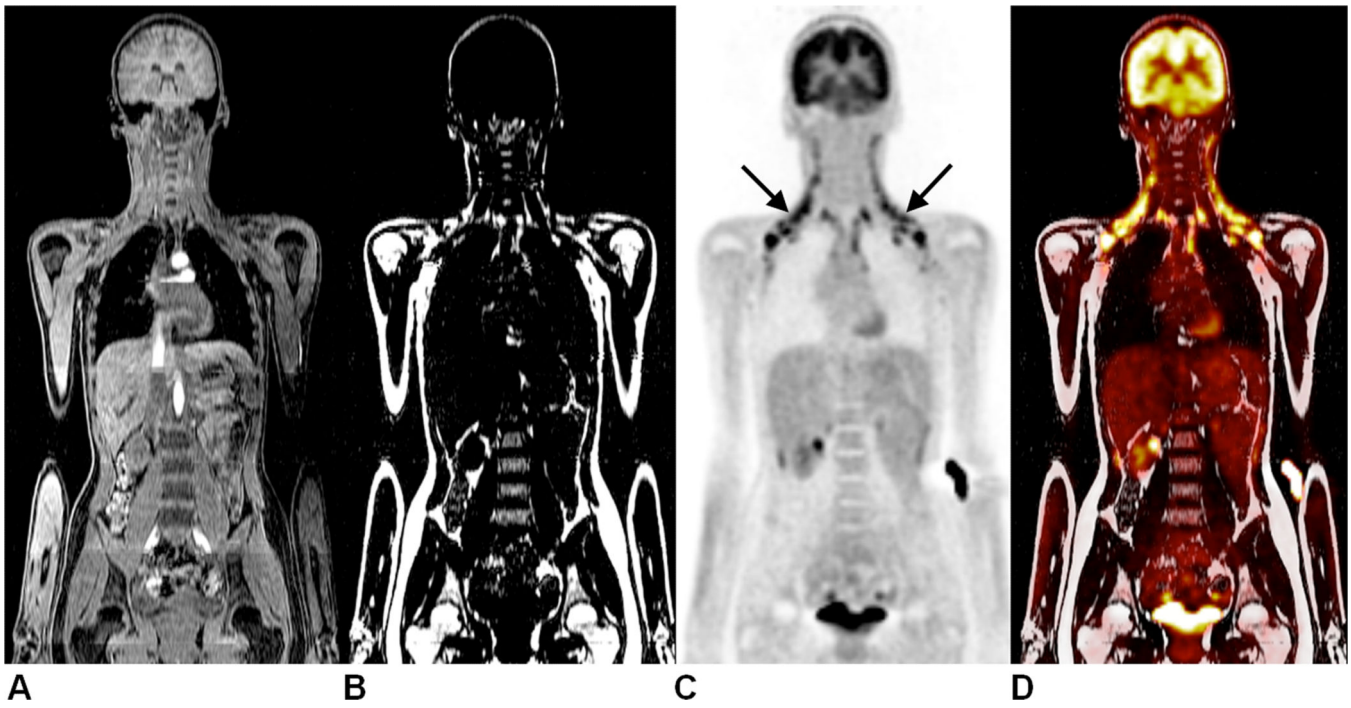

Figure 10.

Representative coronal images from PET/MR of a 15-year old girl presenting for follow-up of Hodgkin's lymphoma. Images illustrate **(A)** water MRI, **(B)** fat MRI, **(C)** PET radiotracer uptake of 18F-FDG, and **(D)** fused PET/fat MRI, with unsuspicious results. However, symmetrical 18F-FDG uptake in the neck (arrows) is evident, and corresponds to the cervical and supraclavicular brown adipose tissue depots on the MR images. Data courtesy of Osman Ratib, M.D., Ph.D., University Hospitals of Geneva, and Benedicte Delattre, Ph.D. and Susanne Heinzer, Ph.D., Philips Healthcare Switzerland.

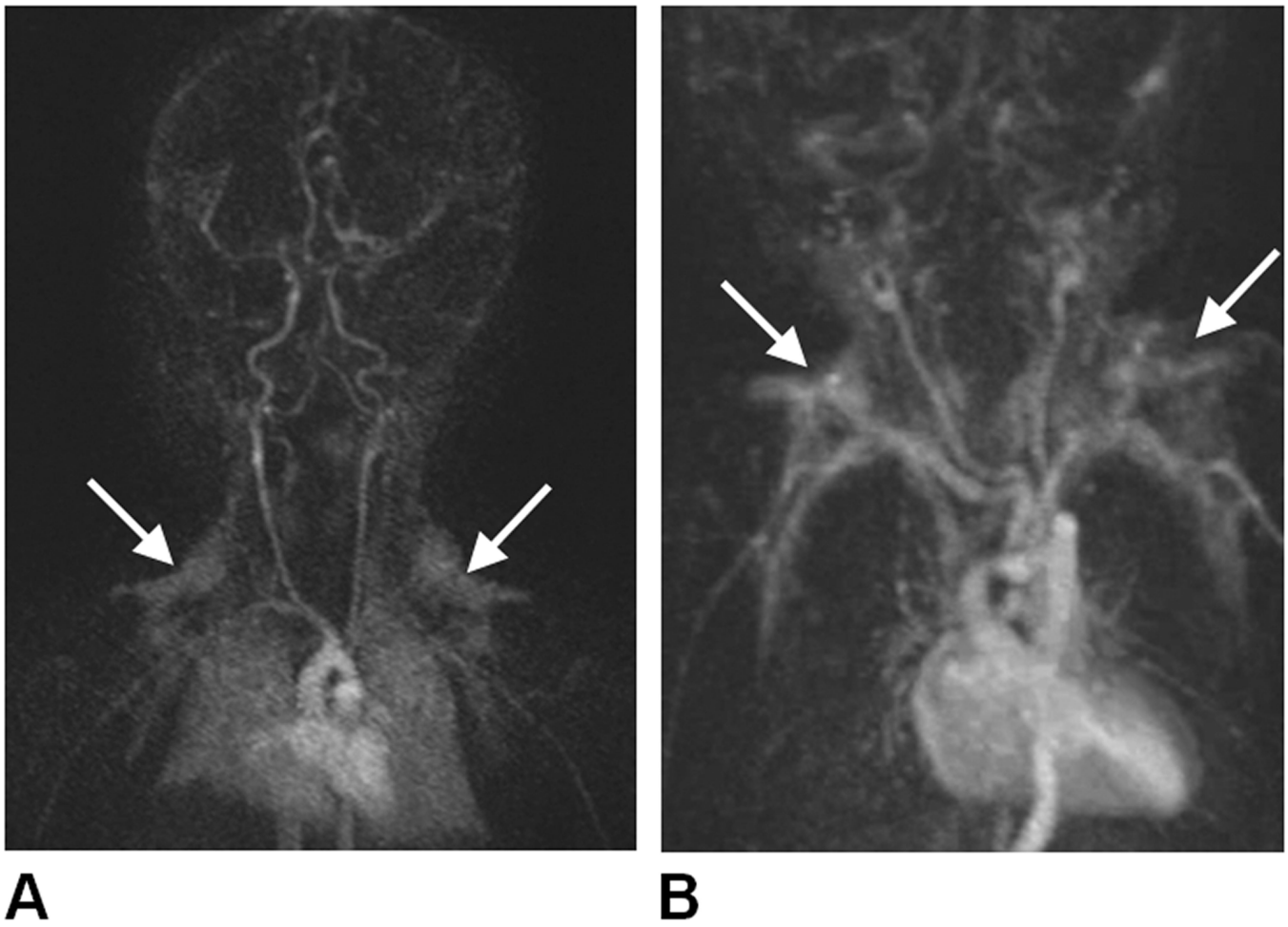

Figure 11.

Coronal maximum-intensity projections of contrast-enhanced MR angiographic acquisitions in two neonates, **(A)**13-day-old male and **(B)** 1-day-old male, illustrating the clear uptake of Gadolinium contrast by the bilateral triangular-shaped supraclavicular fossa brown adipose tissue depots (arrows). Images courtesy of J. Paul Finn, M.D., University of California, Los Angeles.

Table 1

Basis of fat quantification, advantages, disadvantages, and typical applications for T_1-weighted MRI, T_2-weighted MRI, frequency-selective MRI, spectroscopy, and water-fat MRI techniques in fat quantification.

Technique	Basis of Water and Fat Signal Differentiation	Basis of Tissue Signal Contrast	Dimensionality and Typical Pulse Sequence Implementation	Advantages	Disadvantages	Typical Quantitative Endpoints
T_1-Weighted MRI	T_1 longitudinal relaxation	Fat is brighter than water (lean tissue)	2D multi-slice 3D volumetric Spin echo and gradient echo based	• Available on all scanners • Strong water-fat tissue signal contrast • Easy to implement • Rapid breath-hold capable scans • Can be coupled with preparation schemes such as inversion recovery • High spatial resolution	• T_1 contrast varies with B0 field strength, protocols require TR, TE, flip angle optimization to maximize tissue signal contrast • Partial volume effects • Tissue contrast can be sensitive to RF pulse inhomogeneities and hardware imperfections	Volume of adipose tissue depots e.g. SCAT, VAT, intermuscular adipose tissue, bone marrow Detect presence of fat
T_2-Weighted MRI	T_2 transverse relaxation	Fat is brighter than water (lean tissue)	2D multi-slice 3D volumetric Spin echo based	• Available on all scanners • Good water-fat tissue signal contrast • Easy to implement • Can be coupled with preparation schemes such as T_2-prep • High spatial resolution	• T_2 contrast varies with B0 field strength • Partial volume effects • Relatively long scan times • Tissue contrast can be sensitive to RF pulse inhomogeneities and hardware imperfections	Typically not used for adipose tissue depot volumes Detect presence of edema Detect presence of fat Ectopic fat-signal fraction
Frequency-Selective MRI	chemical shift assumes fixed resonance frequency difference between water protons and methylene fat protons	Fat or water is selective excited or suppressed CHEmically Selective Saturation (CHESS) Fat Saturation (FAT-SAT)	2D multi-slice 3D volumetric Spin echo and gradient echo based	• Available on all scanners • Strong water-fat tissue signal contrast via magnetization preparation • Easy to implement • Rapid breath-hold capable scans • Coupled with T_1- and T_2-weighted sequences to increase tissue contrast • High spatial resolution	• Performance varies with B0 field strength • Artifacts can arise from susceptibility to B0 field inhomogeneity	Volume of adipose tissue depots e.g. SCAT, VAT, intermuscular adipose tissue, bone marrow Detect presence of fat Ectopic fat-signal fraction
Single-voxel Spectroscopy (MRS) **Chemical Shift Imaging (CSI)**	chemical shift does not assume fixed or known resonance frequency differences between water and fat protons	Water and fat signals are uniquely identified by their chemical shift locations along the frequency spectrum	1D spectrum 2D multi-slice 3D volumetric spectra STEAM PRESS	• Available option on most scanners • High spectral resolution • Robust water-fat signal identification accurate representation of proton moieties • Characterization of mono-, di- and poly- unsaturated triglycerides • Accurate and sensitive measure of fat-signal fraction, especially at low fat content	• Limited coverage in single-voxel MRS approaches • Moderate spatial resolution in CSI • Voxel boundaries less well defined in CSI • Data analysis may require dedicated software • Moderate scan times	Ectopic fat-signal fraction e.g. liver, pancreas, heart Muscle fat-signal fraction and concentration e.g. IMCL, EMCL
Chemical-Shift-Encoded Water-Fat MRI	chemical shift assumes fixed resonance frequency difference between water and fat protons	Water and fat signals are acquired simultaneously and subsequently separated based on chemical-shift-encoding and fat spectrum modeling	2D multi-slice 3D volumetric Spin echo variants typically used for fat suppression Gradient echo variants typically used for fat quantification IDEAL mDIXON DIXON	• Available option on some scanners • Very strong water-fat tissue signal contrast • Robust water-fat tissue identification and separation • Can be an accurate estimate of proton-density fat fraction • Rapid breath-hold capable scans • High spatial resolution • Can also estimate T_2* and characterize triglyceride composition (e.g. chain length, number of double bonds, etc.)	• Data reconstruction requires specific algorithms that can be computationally intensive • Requires protocol optimization for different B0 field strengths • Water-fat signal swap artifacts can arise from incorrect B0 field map estimation • Not available on all scanners and from all manufacturers	Volume of adipose tissue depots e.g. SCAT, VAT, intermuscular adipose tissue bone marrow Ectopic fat-signal fraction Relaxometry and noise-corrected proton-density fat fraction

Table 2

Select literature reports summarizing progress in MR of BAT morphology and metabolic activity.

MR Technique(s)	First-Author (Ref. Number)	Morphology, Metabolic Activity	Magnetic Field Strength	Rodent, Human	MR Findings	Significance to MR
*** Proton MRS and T_1/T_2-Weighted MRI** **** Proton MRS** ***** Proton MRS and CSI**	* Osculati (181, 182)	Morphology	7.0 Tesla	rodent ex vivo specimen / in vivo	Higher water content in BAT. BAT is consistently hypointense to WAT on conventional MRI.	Difference in fat-to-water ratio of BAT and WAT contributes to difference in signal intensities in MR BAT intensity potentially indicative of underlying adipocyte structure and fat content. Physiology and metabolism-mediated differences in TG properties between BAT and WAT exist and can be quantified by MR.
	** Zancanaro (186)		11.7 Tesla	rodent ex vivo specimen	BAT is more saturated. Unsaturation levels vary with age, temperature, and stimulation.	
	** Strobel (60)		7.0 Tesla	rodent in vivo	BAT and WAT have different water and fat contents. BAT is more saturated than WAT. Measured T_2 of individual TG peaks.	
	** Hamilton (185)		3.0 Tesla	rodent ex vivo specimen	BAT and WAT have different water and fat contents. BAT is more saturated than WAT. Measured T_1 and T_2 of individual peaks.	
	*** Lunati (75)		4.7 Tesla	rodent post-mortem / in vivo	BAT is more polyunsaturated than WAT. Polyunsaturation degree is more uniform in BAT.	
*** T_1/T_2-weighted MRI and Frequency-Selective MRI** **** T_1/T_2- weighted MRI**	* Dundamadappa (179)		not reported	human in vivo	BAT hyperintense versus muscle. BAT signal intensity is variable on fat-suppressed images.	BAT can be visualized on T_1 and T_2 weighted images and exhibit signal intensity differences in comparison to muscle and WAT.
	** Carter (180)				BAT iso- and hyperintense to muscle and hypointense to fat on T_1 and T_2 -weighted images.	
	** Sbarbati (183)	Morphology and Metabolic Activity	4.7 Tesla	rodent in vivo	BAT exhibits lower signals in cold-acclimated animals than those at thermoneutrality. BAT shows decrease in signal after stimulation.	BAT MR signals sensitive to temperature and stimulation.
	* Chen (184)		9.4 Tesla		BAT has a shorter T_2 than WAT, and is less affected by fat-suppression. BAT perfusion visible with MR contrast agent; hemodynamics visible with fMRI.	Characterization of BAT morphology and function is feasible with MR.
*** Proton MRS and Frequency-Selective MRI** **** Frequency-Selective MRI**	* Sbarbati (187)	Morphology	4.7 Tesla		Evident differences in water-fat spectra and signals between muscle, BAT, and WAT.	Works posit and reinforce fat-signal fraction as a useful biomarker for comparing BAT and WAT and for comparing BAT between groups.
	** Lunati (188)				Interscapular BAT has varying fat-signal fractions from surface to intermediate and deep layers.	
	* Peng (189)		7.0 Tesla		Consistent cross-sectional differences in BAT and WAT fat-signal fractions between groups.	
Proton Spectroscopy	Branca (202)		7.0 Tesla	rodent ex vivo specimen / in vivo	Novel approach exploits proximity of water and fat in BAT to generate spectral signal. Relies also on the presence of water and fat in BAT.	Method overcomes intrinsic limitation of spatial resolution and partial-volume effects.
Chemical-Shift-Encoded Water-Fat MRI	Hu (190, 191)		3.0 Tesla	rodent ex vivo specimen / post-mortem / in vivo	BAT consistently occupies a lower and broader fat-signal fraction range than WAT.	Reinforces earlier works that fat-signal fraction contrast between BAT and WAT is potentially a useful biomarker, and that signal trends are consistent between rodents and humans. BAT fat-signal fraction potentially useful in cross-sectional group comparisons.
	Smith (192)		9.4 Tesla	rodent in vivo		
	Holstila (193)		1.5 Tesla	rodent - post-mortem human - in vivo		
	Hu (194, 195, 196)		3.0 Tesla	human post-mortem / in vivo		
	Lidell (197)			human post-mortem		
	Gifford (198)			human in vivo		

MR Technique(s)	First-Author (Ref. Number)	Morphology, Metabolic Activity	Magnetic Field Strength	Rodent, Human	MR Findings	Significance to MR
	Wayte (199)					
	Lundström (200)		1.5 Tesla			
T_2*-weighted MRI	Khanna (228)	Metabolic Activity	7.0 Tesla	rodent in vivo	Variations in BAT metabolic activity due to temperature and drug stimulations are detectable by dynamic T_2* MRI, relying on the BOLD effects of hemoglobin and tissue perfusion.	BAT function and hemo-dynamics can be monitored using MRI, without the use of a contrast agent.
	van Rooijen (201)		3.0 Tesla	human in vivo		
13-Carbon Spectroscopy and CSI	Lau (230)			rodent in vivo	BAT metabolic activity can be quantified with hyperpolarized 13C-pyruvate and its downstream products, bicarbonate, alanine, and lactate.	BAT metabolism and function can be quantified with MR with the administration of emerging exogenous contrast agents.
	Friesen-Waldner (231)					
129-Xenon Spectroscopy and CSI	Branca (232, 233)		9.4 Tesla		BAT metabolic activity can be quantified with 129Xe in gas, lipid-, and cytoplasm-dissolved phases, and the chemical-shift of 129Xe due to temperature.	